

# X-Ray Spectral Variability of the Seyfert Galaxy NGC 4051 Observed with *Suzaku*

Yuichi TERASHIMA<sup>1</sup>, Luigi C. GALLO<sup>2</sup>, Hirohiko INOUE<sup>3,4</sup>, Alex G. MARKOWITZ<sup>5</sup>, James N. REEVES<sup>6</sup>, Naohisa ANABUKI<sup>7</sup>, Andrew C. FABIAN<sup>8</sup>, Richard E. GRIFFITHS<sup>9</sup>, Kiyoshi HAYASHIDA<sup>7</sup>, Takeshi ITOH<sup>10</sup>, Norihide KOKUBUN<sup>3</sup>, Aya KUBOTA<sup>11</sup>, Giovanni MINIUTTI<sup>12</sup>, Tadayuki TAKAHASHI<sup>3,10</sup>, Makoto YAMAUCHI<sup>13</sup>, and Daisuke YONETOKU<sup>14</sup>

<sup>1</sup>Department of Physics, Ehime University, 2-5 Bunkyo-cho, Matsuyama, Ehime, 790-8577

<sup>2</sup>Department of Astronomy and Physics, Saint Mary's University, Halifax, NS B3H 3C3, Canada

<sup>3</sup>Institute of Space and Astronautical Science, Japan Aerospace Exploration Agency, 3-1-1 Yoshinodai, Sagami-hara, Kanagawa 229-8510

<sup>4</sup>Department of Physics, Tokyo Institute of Technology, 2-12-1 Ohokayama, Meguro, Tokyo 152-8551, Japan

<sup>5</sup>Center for Astrophysics and Space Sciences, University of California, San Diego, M.C.0424, La Jolla, CA 92093-0424, USA

<sup>6</sup>Astrophysics Group, School of Physical and Geographical Sciences, Keele University, Keele, Staffordshire ST5 8EH, UK

<sup>7</sup>Department of Earth and Space Science, Osaka University, Toyonaka, Osaka 560-0043, Japan

<sup>8</sup>Institute of Astronomy, University of Cambridge, Madingley Road, Cambridge CB3 0HA, UK

<sup>9</sup>Department of Physics, Carnegie Mellon University, 5000 Forbes Avenue, Pittsburgh, PA 15213, USA

<sup>10</sup>Department of Physics, The University of Tokyo, 7-3-1 Hongo, Bunkyo, Tokyo 113-0033

<sup>11</sup>Department of Electronic Information Systems, Shibaura Institute of Technology, 307 Fukasaku, Minuma-ku, Saitama-shi, Saitama 337-8570

<sup>12</sup>Laboratoire APC, UMR 7164, 10 rue A. Domon et L. Duquet, 75205 Paris, France

<sup>13</sup>Department of Applied Physics, University of Miyazaki, 1-1 Gakuen-Kibanadai-Nishi, Miyazaki, Miyazaki 889-2192

<sup>14</sup>Department of Physics, Kanazawa University, Kakuma-machi, Kanazawa 920-1192, Japan

(Received ; accepted )

## Abstract

We report results from a *Suzaku* observation of the narrow-line Seyfert 1 NGC 4051. Broad-band X-ray light curves and spectra in the 0.4–40 keV band are examined. During our observation, large amplitude rapid variability is seen and the averaged 2–10 keV flux is  $8.1 \times 10^{-12}$  erg s<sup>−1</sup> cm<sup>−2</sup>, which is several times lower than the historical average. The X-ray spectrum hardens when the source flux becomes lower, confirming the trend of spectral variability known for many Seyfert 1 galaxies. The broad-band averaged spectrum and spectra in high and low flux intervals are analyzed. The spectra are first fitted with a model consisting of a power-law component, a reflection continuum originating in cold matter, a blackbody component, two zones of ionized absorber, and several Gaussian emission lines. The amount of reflection is rather large ( $R \sim 7$ , where  $R = 1$  corresponds to reflection by an infinite slab), while the equivalent width of the Fe-K line at 6.4 keV is modest (140 eV) for the averaged spectrum. We then model the overall spectra by introducing partial covering for the power-law component and reflection continuum independently. The column density for the former is  $1 \times 10^{23}$  cm<sup>−2</sup>, while it is fixed at  $1 \times 10^{24}$  cm<sup>−2</sup> for the latter. By comparing the spectra in different flux states, we identify the causes of spectral variability. At high energies (>3.5 keV) the primary cause of the spectral variability is the change of the normalization of the power-law component with a constant photon index ( $\Gamma = 2.04$ ) overlaid on a nearly constant hard component. The constant hard component is interpreted as partially covered reflection. At lower energies, variations in the covering fraction of the power-law continuum is an additional cause of spectral variability.

**Key words:** X-rays: galaxies — galaxies: active — galaxies: individual (NGC 4051)

## 1. Introduction

NGC 4051 is an X-ray bright, nearby ( $z = 0.00234$ ) narrow-line Seyfert 1 galaxy. Its X-ray flux and spectral shape, which have been studied with major X-ray satellites, are highly variable both on short (< day) and long (years) timescales. Such spectral variability can be used to extract the various emission components and to understand the physical origin of the variability. Rapid flux and spectral variability within a few hundred sec-

onds have been known since observations with *EXOSAT* (Lawrence et al. 1985) and then *Ginga* (Matsuoka et al. 1990, Kunieda et al. 1992). Extensive long-term monitoring by *RXTE* showed that this object displays large amplitude variability and occasionally enters periods of very low flux (Uttley et al. 1999; Markowitz & Edelson 2004).

The trend of the spectral variability above a few keV is that the spectrum flattens when the flux becomes lower. In a high flux state, its spectrum in the 0.5–10 keV band

is typical of that seen for Seyfert 1s, consisting of a power-law component, an Fe-K line, a reflection continuum originating in cold matter, a soft excess, and ionized absorbers (e.g., Pounds et al. 2004 for an *XMM-Newton* observation in 2001). When the source became fainter, the hard band spectrum above  $\sim 2$  keV significantly flattened and a component with a convex shape was seen (Uttley et al. 2004, Pounds et al. 2004, Ponti et al. 2006, Gallo 2006 for an *XMM-Newton* observation in 2002 Nov.; Uttley et al. 2003 for the *Chandra* observation in 2001 Feb.). This component was interpreted as a relativistically broadened Fe-K line (Uttley et al. 2003), a combination of reflection from an ionized disk and a Fe-K line, both blurred by relativistic effects (Ponti et al. 2006), or a primary continuum partially covered by a weakly ionized absorber ( $\xi \approx 25$  erg cm s $^{-1}$ , Pounds et al. 2004).

NGC 4051 occasionally enters a very low flux state. Such an event was observed by *RXTE* and *BeppoSAX* in 1998, with an X-ray flux of  $1.3 \times 10^{-12}$  erg s $^{-1}$ cm $^{-2}$  in the 2–10 keV band. The observed X-ray spectrum was very flat ( $\Gamma \approx 0.8$ ) and accompanied by a strong Fe-K line with an equivalent width ( $EW$ )  $\approx 600$  eV, consistent with a reflection-dominated spectrum. This spectrum is consistent with the idea that the nuclear activity had switched off and that the observed X-rays were reflected from matter located far from the nucleus and possibly identified with the molecular torus (Guainazzi et al. 1998, Uttley et al. 1999).

Several different interpretations for the observed spectral variability have been proposed. A first possibility is that the spectral variability is mainly caused by an intrinsic change of the power law slope. Guainazzi et al. (1996) analyzed spectral variability using *ASCA* data obtained in 1994 and found that the power law slope changed by  $\Delta\Gamma = 0.4$  if the normalization of the reflection component is constant or inversely proportional to the normalization of the power-law component. Lamer et al. (2003) analyzed long-term spectral variability using *RXTE* data and found that the slope of the power-law component varies even after subtracting a reflection component, which is assumed to be constant. Taylor et al. (2003) performed flux-flux analysis for *XMM-Newton* data using the two energy bands 2–5 keV and 7–15 keV, and concluded that the spectral variability is described by a pivoting power-law component (i.e., change of the power law slope) superimposed on a constant hard component. Uttley et al. (2004) analyzed flux-flux plots in the 0.1–0.5 keV and 2–10 keV bands for high and low flux states observed with *XMM-Newton* in 2002 Nov. and reached a similar conclusion. They explained the spectral variability by a power-law component with a varying photon index combined with constant thermal and reflection components, confirming the interpretation of *Chandra* results by Uttley et al. (2003).

A second scenario is a two-component model consisting of a soft variable component and a hard constant component. Ponti et al. (2006) explained the spectral variability observed with *XMM-Newton* in 2001 and 2002 with this two-component model, in which a power law with

a fixed photon index ( $\Gamma = 2.2$ ) was used as the variable component. A combination of ionized reflection blurred by a Laor (1991) kernel and neutral reflection from distant matter was introduced as the constant component. The former is interpreted as constant in the context of the light bending effect around the central Kerr black hole (Miniutti & Fabian 2004).

Pounds et al. (2004) analyzed the same *XMM-Newton* data and interpreted the variability using the two-component model combined with the presence of an absorbed component. They assumed that the strength of the reflection component and the photon index of the power-law component were same between the two observations and interpreted the very hard spectrum observed in 2002 by a combination of a significant contribution of a 'constant' cold reflection component and an increased column density of absorption with a low ionization state.

Spectral variability has been thus interpreted by various combinations of a pivoting power-law component, a constant flat component, and absorption, and the underlying physics is yet to be understood. A powerful way to decompose these various components and to extract the variable component(s) is time-resolved broad-band spectroscopy. NGC 4051 is bright at energies above 10 keV and detected by *Ginga* (up to 20 keV; e.g., Matsuoka et al. 1990, Awaki et al. 1991, Kunieda et al. 1992), *BeppoSAX* (up to 50 keV in a low flux state, Guainazzi et al. 1998), *INTEGRAL* (over 17–60 keV, Sazonov et al. 2007, Krivonos et al. 2007, Beckmann et al. 2006), and *Swift* (in the 14–195 keV band, Tueller et al. 2008). It is therefore one of ideal targets to study the nature of broad-band spectral variability with *Suzaku*, which achieves broad-band coverage up to 40 keV with a good signal-to-noise ratio for sources with a moderate flux. Indeed, the variable emission component in Seyferts has been successfully measured in *Suzaku* observations to be a power law with a constant photon index (MCG–6-30-15, Miniutti et al. 2007; MCG–5-23-16, Reeves et al. 2007; NGC 4388, Shirai et al. 2008; NGC 4945, Itoh et al. 2008).

In this paper, we present the results of analysis of spectral variability of NGC 4051 using *Suzaku* to decompose the variable and constant emission components. This paper is organized as follows: Section 2 describes the observation and data reduction. Section 3 and 4 describe light curves and spectra, and the results are discussed in Section 5. Section 6 summarizes our findings.

## 2. Observation and Data Reduction

NGC 4051 was observed with *Suzaku* on 2005 Nov. 10–13 as a part of the Science Working Group observations. *Suzaku* (Mitsuda et al. 2007) carries four X-ray telescopes (XRTs, Serlemitsos et al. 2007), with four X-ray CCD cameras (X-ray Imaging Spectrometer XIS, Koyama et al. 2007) at the focal plane of the XRTs, and a non-imaging Hard X-ray Detector (HXD, Takahashi et al. 2007). Three of the four XISs (XIS0, 2, 3) are front-illuminated (FI) CCDs and the other one (XIS1) is a back-illuminated CCD, and has larger quantum efficiency at lower ener-

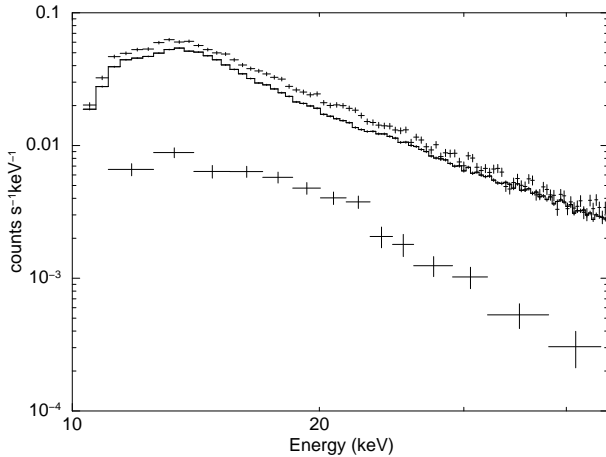


**Fig. 1.** HXD/PIN spectra of NGC 4051. The total observed spectrum is denoted by the upper data points. The non-X-ray background + Cosmic X-ray background are denoted by the middle data points, using a solid histogram. The lower data points denote the background-subtracted spectrum.

gies compared to the FI CCDs. The HXD consists of Si PIN diode (PIN) and GSO scintillators surrounded by BGO active shields. The XIS and HXD are co-aligned and NGC 4051 was placed at the HXD nominal pointing position in this observation.

The four XISs were operated in  $5 \times 5$  or  $3 \times 3$  editing modes combined with normal clocking mode. We used cleaned events from the version v1.2 pipeline processing data. Time intervals in which telemetry saturation occurred were excluded by applying the good time intervals provided by the XIS team. Since NGC 4051 is highly variable and a main purpose of our analysis to understand the spectral variability in this object, we selected only time intervals where data from the XIS and HXD/PIN were taken simultaneously. The effective exposure after the data screening was 81.6 ksec for each XIS. The mean count rates are  $0.46 \text{ counts s}^{-1}$  per each FI sensor and  $0.69 \text{ counts s}^{-1}$  per BI sensor in the  $0.4\text{--}10 \text{ keV}$  band. Response matrices and ancillary response files were made for each XIS using `XISRMFGN` and `XISSIMARFGN`, respectively. Light curves and spectra were extracted from a circular region with a radius of  $2'.9$  arcmin. Background spectra were accumulated from an annular region centered on the target and a region around a nearby source was excluded.

The cleaned event file from the version 1.2 pipeline processing was used for analysis of the HXD data. In this paper we analyze only the data from the PIN because no significant signals were detected from the GSO. Deadtime correction was done for PIN spectra and light curves. Only the data taken simultaneously with the XIS were used. The effective exposure after data screening was 81.6 ksec (before deadtime correction) or 76.6 ksec (after deadtime correction). The response matrix appropriate for the date of this observation and version 1.2 processing (`ae_hxd_pinhxnom.20060814.rsp`) was used in spectral fits.

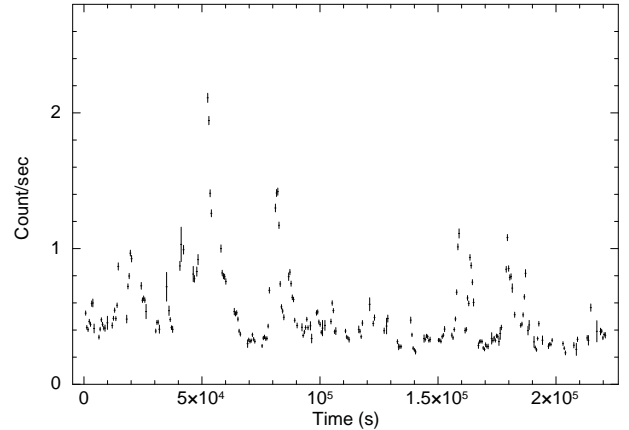


**Fig. 2.** The light curve in the  $0.5\text{--}10 \text{ keV}$  band obtained with the XIS, using a bin size of 512 sec. The data from the four XIS sensors are combined.

The non-X-ray background (NXB) appropriate for the version 1.2 products provided by the HXD team was subtracted from spectra and light curves, after the same time intervals as the actual data was selected. We assumed the shape of the spectrum of the cosmic X-ray background (CXB) presented in Boldt (1987) and Gruber et al. (1999) and simulated an expected spectrum of the CXB using the response file for a flat field with an area of  $2^\circ \times 2^\circ$  by using `XSPEC`. The form of the CXB is expressed as  $9.0 \times 10^{-9} (E/3 \text{ keV})^{-0.29} \exp(-E/40 \text{ keV}) \text{ erg cm}^{-2} \text{ s}^{-1} \text{ str}^{-1} \text{ keV}^{-1}$ , or  $9.41 \times 10^{-3} (E/1 \text{ keV})^{-1.29} \exp(-E/40 \text{ keV}) \text{ photons cm}^{-2} \text{ s}^{-1} \text{ keV}^{-1} (2^\circ \times 2^\circ)^{-1}$ . The spectra of the NXB and CXB were combined, and then subtracted from the on-source spectrum. The spectra of the NXB+CXB and data before and after background subtraction are shown in Fig. 1. The count rates of the signal are more than 10% of those of the NXB up to  $\sim 40 \text{ keV}$ . The uncertainties of flux measurements with HXD/PIN are dominated by the systematic error of the NXB estimation. For example, the  $1\sigma$  systematic error for an observation with a duration of one day is  $\approx 2\%$  if statistical errors are subtracted in quadrature (Fig. 3 in Mizuno et al. 2007). Detection is therefore significant at more than  $5\sigma$  level in the  $15\text{--}40 \text{ keV}$  band. The accuracy of the background subtraction can be tested by comparing the data taken during the field of view is occulted by the earth with the NXB. Such time intervals, however, did not exist in this particular observation. We therefore assumed the systematic error of the NXB estimation given in Mizuno et al. (2007) without any further tuning.

### 3. Variability

#### 3.1. Light Curves

The light curve in the  $0.5\text{--}10 \text{ keV}$  band obtained with the XIS is shown in Fig. 2. The bin size is 512 sec, and the data from the four XIS sensors are combined. The origin of time is 2005 Nov. 10, 20:12:02 (UT). During our observation, NGC 4051 showed several flare-like time variations within a few thousand seconds. The amplitudes of these

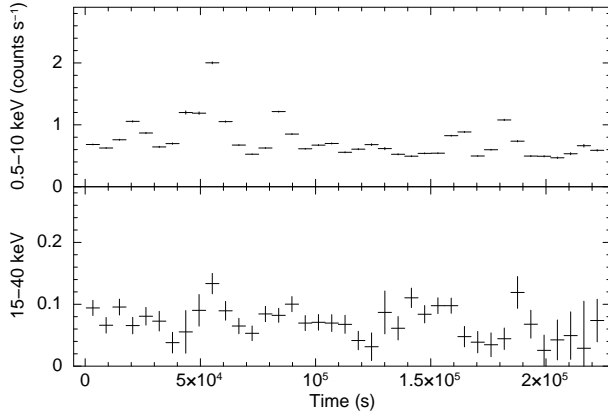


**Fig. 3.** (Upper) The light curve in the 0.5–10 keV band obtained with the XIS. The bin size is 5760 sec. The data from the four XIS sensors are combined. (Lower) The light curve in the 15–40 keV band obtained with the HXD PIN. The bin size is 5760 sec. The deadtime has been corrected. The NXB has been subtracted. The  $1\sigma$  systematic error on the PIN count rates is  $\sim 0.017 \text{ c s}^{-1}$ .

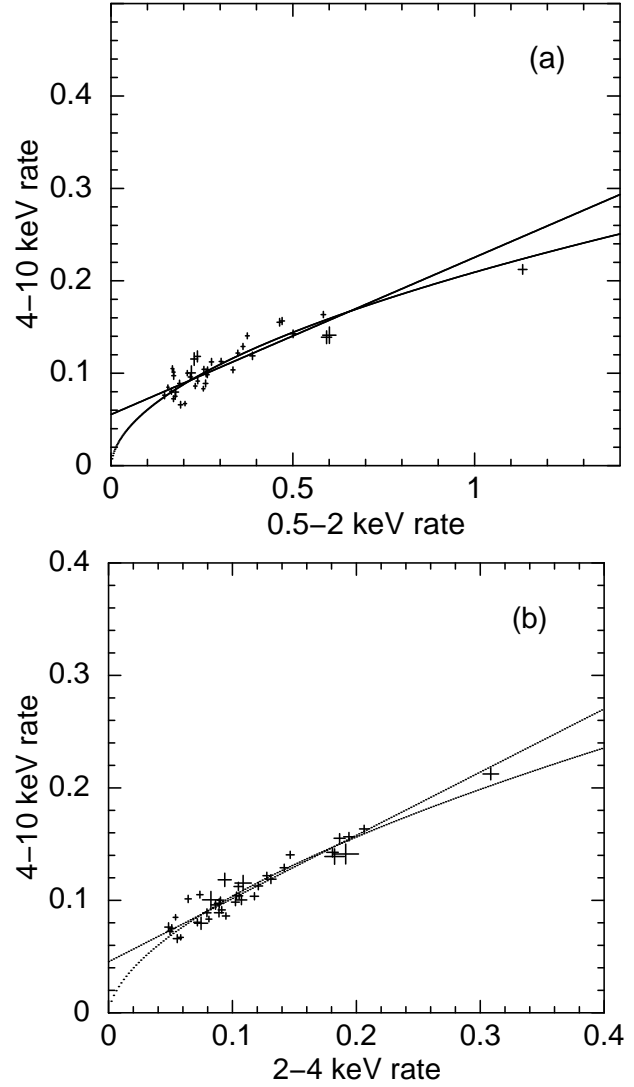
flares are about a factor of 2–5.

The light curve in the 15–40 keV band obtained with the HXD PIN is compared with that in the 0.5–10 keV band in Fig. 3. The XIS light curve in the 0.5–10 keV band and PIN light curve in the 15–40 keV band are shown in the top and bottom panels, respectively. The bin size is 5760 sec and the origin of time is 2005 Nov. 10, 20:55:43 (UT). Deadtime correction was done for the PIN light curves. The hard X-ray flux from the Cosmic X-ray background ( $\sim 0.013 \text{ ct s}^{-1}$  in the 15–40 keV band) was not subtracted, while the NXB was subtracted in the lower panel of Fig. 2. Only statistical errors are included as the error bars. The systematic error is about 6.0% of the NXB flux level ( $0.28 \text{ ct s}^{-1} \times 0.06 \approx 0.017 \text{ c s}^{-1}$ ) at  $1\sigma$  for a time bin of  $\sim 6 \text{ ksec}$  (Mizuno et al. 2007). It is clear from the figure that the variability amplitude is much lower in the harder band and that the flux in the hard band is only mildly variable.

### 3.2. Flux-Flux Correlations

In order to characterize the spectral variability, we made flux-flux plots for several energy bands. In Fig. 4(a) and (b), the count rates in the 4–10 keV band are plotted against the count rates in the 0.5–2 keV and 2–4 keV bands, respectively, while the 15–40 keV and 2–10 keV bands are compared in Fig. 4(c). The data from the four XIS sensors were combined. A bin size of 5760 sec was used for Fig. 4(a) and (b), while the bin size for Fig. 4(c) was 23040 sec. These figures show that the amplitude of variability becomes smaller as the energy band becomes harder. Such trends are also demonstrated by root-mean-square spectra, shown in the next subsection.

We fit the flux-flux plots with a linear function and found that there is an offset in the hard (4–10 keV) band. The offsets for Fig. 4(a) and (b) are  $0.056 \text{ ct s}^{-1}$  and  $0.046 \text{ ct s}^{-1}$ , respectively. The best-fit lines are shown in Fig. 4.



Under the assumption that a linear relationship accurately characterizes the intrinsic flux-flux relation, the hard offset indicates that there is a constant component with a hard spectrum and that variability is mainly caused by a change of normalization of a spectral component of nearly constant spectral shape. Such a two-component behavior has been suggested based on *XMM-Newton* observations except for time intervals with a very low flux (Ponti et al. 2006).

The data points in Fig. 4(a) may show a slight convex curvature compared to the best-fit linear solution. We therefore compared the data to a model consisting of a power law and obtained a better description ( $\chi^2 = 495$  (power law) versus 554 (linear) for 37 degrees of freedom). The exponent of the power law is 0.54, which is near the value 0.642 obtained by Taylor et al. (2003) for the two energy bands 2–5 keV and 7–15 keV using *RXTE*. The best-fit models are also shown in Fig. 4(a). Under the assumption that the intrinsic flux-flux relation is characterized by a power law, this result would suggest that the main cause of spectral variability depends on the energy

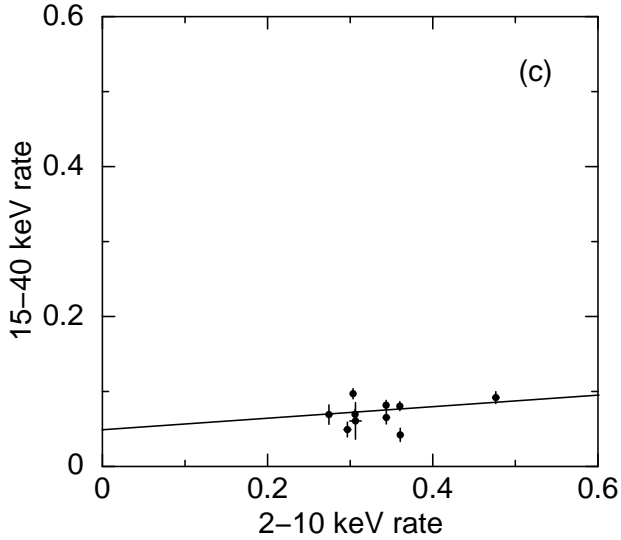


**Fig. 4.** Flux-flux plots. The solid and dashed lines represent best-fit linear and power-law functions, respectively. (a) 4–10 keV and 0.5–2 keV bands. The time bin size is 5760 sec. (b) 4–10 keV and 2–4 keV bands. The time bin size is 5760 sec. (c) 15–40 keV and 2–10 keV bands. The time bin size is 23040 sec.

band and that the change of the intrinsic spectral shape is play a role in addition to the two-component model. Taylor et al. (2003) and Uttley et al. (2004) applied a power law type model to their flux-flux plots, and spectral pivoting was implied to be the main cause of spectral variability. The comparison between the data points and the model functions shown in Fig. 4 (a) and (b), along with the very large  $\chi^2$  values, suggest that neither linear nor power-law models offer a complete description of the observed flux-flux relation. Indeed, detailed spectral analysis presented below demonstrates the importance of modeling the variability of the absorbing material, particularly at energies below  $\sim 4$  keV.

A flux-flux plot for harder energies is shown in Fig. 4(c) and indicates that the amplitude of variability is very small in the hard band 15–40 keV. Note that the  $1\sigma$  systematic error in estimating the HXD background is about 4% of the NXB, which corresponds to  $0.01 \text{ ct s}^{-1}$ , for a duration of  $\sim 20$  ksec (Mizuno et al. 2007), and that the true amplitude is smaller than the scatter in the vertical direction in Fig. 4(c). This flux-flux plot is consistent with the two-component picture, in which the harder X-ray band is dominated by a nearly constant component with a hard spectrum.

### 3.3. RMS spectra

Fractional variability amplitudes in excess of the noise were calculated for light curves in narrow energy bands and plotted against energy. Such an RMS spectrum is a useful way to quantify spectral variability (e.g., Vaughan et al. 2003, Markowitz et al. 2003). We used the definition and error of the fractional root mean square variability amplitude ( $F_{\text{var}}$ ) shown in Vaughan et al. (2003). RMS spectra were calculated for two time bin sizes, 1024

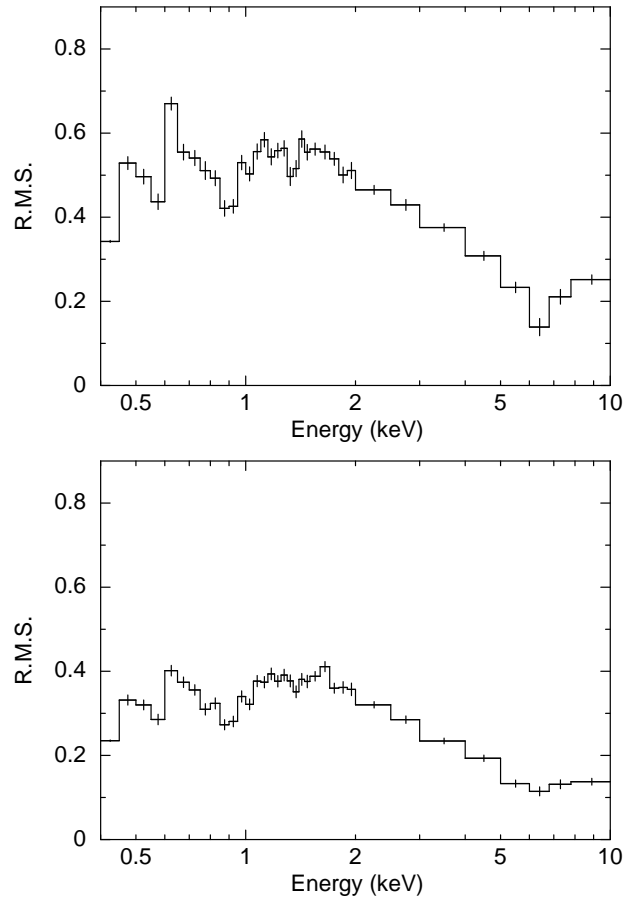


**Fig. 5.** The root mean square spectrum. (a) The time bin size is 1024 sec. (b) The time bin size is 20480 sec.

and 20480 sec, and are shown in Fig. 5. The overall shape is such that the RMS value is peaking at around  $\sim 0.6 - 1$  keV and then gradually decreases toward higher energies. Such a shape peaking near 1–2 keV is known for some Seyfert 1 galaxies (MCG–6-30-15, Vaughan & Fabian 2004; Mrk 766, Arévalo et al. 2008; 1H0707–495, Fabian et al. 2004, Gallo et al. 2004; IRAS 13224–3809, Gallo et al. 2007). Several sharp drops are also clearly seen at 0.58, 0.90, 1.35, and 6.4 keV, thanks to the good energy resolution of the XIS at low energies and the high variability-to-noise ratios in this source. These energies coincide with emission lines seen in the spectra as shown below and can be identified with K-shell lines from O VII, Ne IX, Mg XII, and neutral or low ionization Fe, respectively. Such sharp features are not clear in an RMS spectrum measured from a high flux state observation in 2001, while a dip at 0.9 keV has been observed in an RMS spectrum of a low flux state in 2002 (Ponti et al. 2006). Other lines are less clear in the previous RMS spectra, though localized decreases in the RMS around 0.5 keV, 1.3 keV, and 6.5 keV are seen.

#### 4. Spectral Variability

We divided the data into high and low flux states to study spectral variability, where a threshold of 0.65 counts  $\text{s}^{-1}$  per XIS0 was used. In order to extract variable components, we first made a difference spectrum between the high and low flux states, and then examined spectra of each flux level (high and low) as well as the averaged spectrum. The three XIS-FI spectra were co-added. Response matrices and ancillary response files for these three XIS-FI sensors were combined using ADDRMF and ADDARF, respectively. We fitted the XIS-FI, XIS-BI, and PIN spectra simultaneously, though only XIS-FI and PIN data are shown in figures below for clarity, unless otherwise noted. In fitting XIS and HXD PIN spectra, we assumed that the relative normalizations of XIS0+2+3, XIS1, and PIN was 1:0.96:1.16 based on version 1.2 data of the Crab nebula analyzed by the *Suzaku* X-ray Telescope team.

The XIS and HXD/PIN background-subtracted spectra were fitted using XSPEC v11.3. The spectra were binned so that each bin contains at least 30 counts and the chi-squared minimization technique could be used to fit the spectra. The energy band 1.8–1.9 keV of the XIS spectra was ignored in the spectral fits to avoid residual calibration uncertainties known in this band. The hydrogen column density of the Galactic absorption  $N_{\text{H}} = 1.2 \times 10^{20} \text{ cm}^{-2}$  (Kalberla et al. 2005) obtained by the tool *nh* in the HEASOFT 6.3.1 package was included in the spectral models described below. All errors quoted are at 90% confidence for one parameter of interest ( $\Delta\chi^2 = 2.7$ ).

Spectra of the  $^{55}\text{Fe}$  calibration sources in the XIS cameras were extracted to quantify residual calibration uncertainties. We fitted the spectra around the peak of the Mn-K $\alpha$  line with a Gaussian component and measured the peak energy and width  $\sigma$ . The measured line energies were within 5 eV of the expected energy. The widths were consistent with zero. The largest residual width is seen in XIS3 ( $\sigma \approx 11$  eV). We therefore estimate that the uncertainties in the energy and width are less than  $\sim 5$  eV and  $\sim 10$  eV for the simultaneous fits presented below.

##### 4.1. Difference Spectrum

The spectrum in the low flux state was subtracted from that in the high flux state to make a difference spectrum. Since the background of the XIS is stable and similar background count rates are expected for spectra in both states, we used XIS spectra without background subtraction. Errors in each spectral bins were propagated. On the other hand, the background of the PIN is highly time-dependent, and therefore we prepared background-subtracted spectra for both states, and then a difference spectrum was made using them. Errors were propagated in each arithmetic operation.

The difference spectrum thus obtained is shown in Fig. 6. We first fit this spectrum using a simple power law model without any modifications by absorption in the 3–40 keV band. The spectrum is well fitted with a power law with a photon index of  $2.04 \pm 0.16$  ( $\chi^2/\text{dof}$  was 18.8/47) and no systematic residuals are seen. The best-fit power

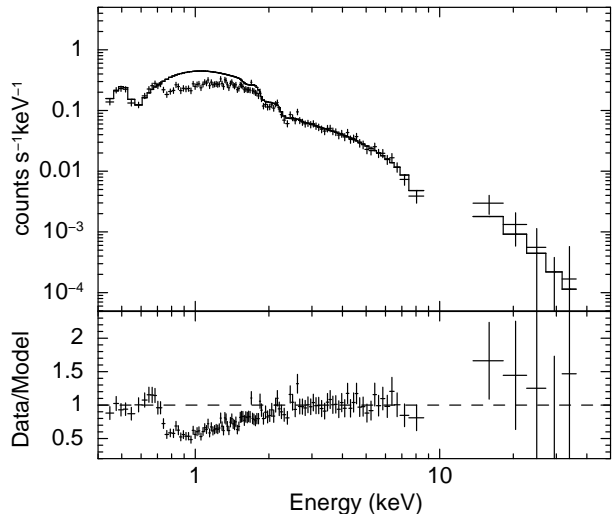


**Fig. 6.** The difference spectrum between the high and low flux states. XIS 1 data are not shown for clarity, though they were used in the spectral fits. The upper panel shows the difference spectrum (crosses) and the best-fit power law model in the 3–40 keV band extrapolated to energies below 3 keV (histogram). The lower panel shows data/model ratio.

law model extrapolated to lower energies is also shown in Fig. 6. Absorption due to the Galactic column ( $N_{\text{H}} = 1.2 \times 10^{20} \text{ cm}^{-2}$ ) is applied in this figure. The data in the 0.7–2 keV band are located below the extrapolation of the power law and indicate the presence of absorption in this energy band.

Next we added a narrow ( $\sigma = 10$  eV) Gaussian at 6.4 keV in the source rest frame to set a limit on the variability of the Fe-K emission line. The 90% confidence upper limit of the equivalent width ( $EW$ ) is 160 eV. The presence of a reflection component was also examined. We used the PEXRAV component in XSPEC (Magdziarz & Zdziarski 1995) to constrain the strength of the reflection ( $R$  or *rel\_refl* in the PEXRAV component) from cold matter.  $R$  is the reflection fraction, defined as  $R = \Omega/2\pi$ , where  $\Omega$  is the solid angle of a cold reflector viewed from an X-ray source. An inclination angle of  $i = 45^\circ$  and an incident spectrum consisting of a power law with an exponential cutoff energy of 300 keV were assumed in the fits. The photon index and  $R$ , however, are strongly coupled with each other and no meaningful constraint was obtained. If we fixed the photon index at 2.04, the upper limit on  $R$  became 1.7 ( $\Delta\chi^2 = 2.7$ ) or 2.1 ( $\Delta\chi^2 = 4.6$ ), which are consistent with the absence of strong reflection, although these constraints are not tight.

##### 4.2. Spectral Ratio

The difference spectrum in the previous section suggests the presence of variable absorption. Since absorption is a multiplicative component, a ratio of the low flux to high flux spectra is useful to see the effect of absorption. We therefore made such a ratio plot (low flux/high flux states), shown in Fig. 7. A few absorption models are also shown in Fig. 7, in which we assumed that the shape of

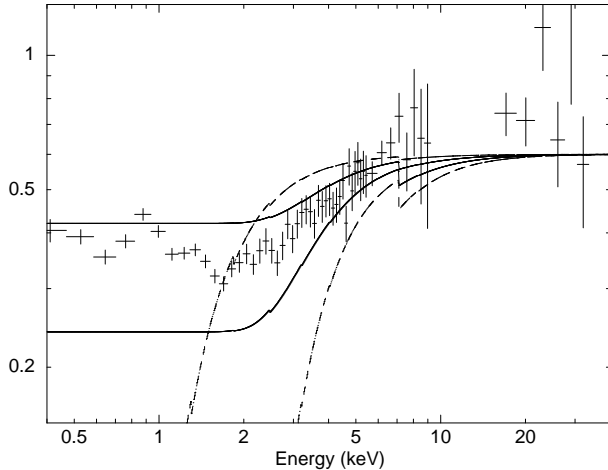


**Fig. 7.** Ratio of the low flux state to high flux state spectra. The upper and lower dashed lines are the ratios expected for absorption by neutral matter with a column density of  $N_H = 10^{22} \text{ cm}^{-2}$  and  $10^{23} \text{ cm}^{-2}$ , respectively. Upper and lower solid lines are the ratios expected for partial covering absorption with covering fractions of 0.3 and 0.6, respectively, where a column density of  $N_H = 10^{23} \text{ cm}^{-2}$  is assumed. In these models, the continuum flux is assumed to be reduced by 40% in the low flux state.

the underlying continuum remains the same, and the normalization of the continuum is reduced by 40% in the low flux state compared to the high flux state. The upper and lower dashed lines in Fig. 7 are the ratios expected for absorption by neutral matter with a column density of  $N_H = 10^{22} \text{ cm}^{-2}$  and  $10^{23} \text{ cm}^{-2}$ , respectively. The energy dependence of the ratio data is shallower than these curves in that the data points lie much higher than the models at low energies (below 2 keV). This fact indicates that a simple neutral absorber does not explain the observed spectral variability. The ratios expected for partial covering absorbers with covering fractions of 0.3 and 0.6 are also shown as upper and lower solid lines, respectively, in Fig. 7, where a column density of  $N_H = 10^{23} \text{ cm}^{-2}$  was assumed. Both sets of model points are nearly flat at energies below  $\sim 3 \text{ keV}$ . The fact that they are similar in spectral shape to the observed ratio spectrum at low energies suggests the presence in NGC 4051 of less absorbed components, which might be modeled using partial covering. Full details of absorption models are explored in the following subsections.

#### 4.3. Spectra in the 3.5–40 keV band

##### 4.3.1. Empirical Two-component Model

The result of spectral fits to the difference spectrum in the previous subsection suggests that the variable component in the hard energy band above 3 keV is dominated by a power-law component, and that the total spectrum consists of a power-law component plus a harder constant component. We adopt a reflection continuum expected from cold matter, which is often present in spectra of Seyfert 1s, as the hard component. The spectra in the two flux states were fitted with a model consisting of a

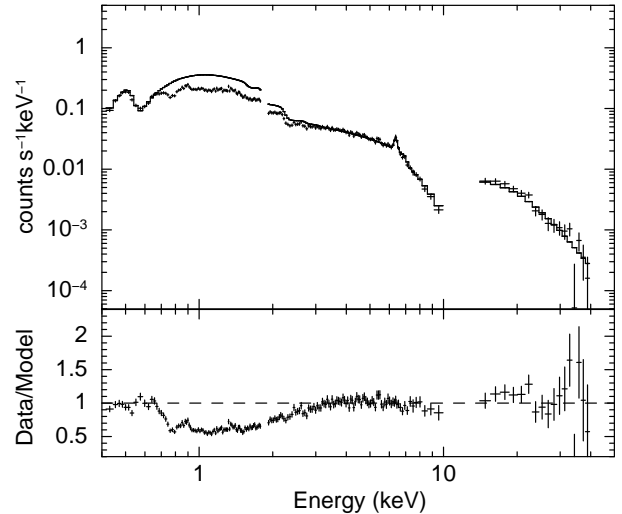


**Fig. 8.** The averaged spectrum fitted with the two-component model in the 3.5–40 keV band. The best-fit model (solid histogram) is extrapolated to lower energies. The lower panel shows data/model ratio.

power-law component and a reflection continuum. The photon index of the power-law component was fixed at 2.04, determined by the fit to the difference spectrum. The PEXRAV component in XSPEC was used as the shape of the reflection continuum, with the parameter `rel_refl` fixed at  $-1$ , meaning that this component was used purely to model reflection and not the flux associated with the incident power-law component. Gaussian components were added if emission/absorption features were seen. This model hereafter is referred to as Model-A1. The shape of the continuum is well fitted with this model for the flux states analyzed here. The data and best-fit model for the averaged spectrum is shown in Fig. 8 as an example. The model extrapolated to lower energies is also presented in the same figure. The spectral parameters of the fits in the 3.5–40 keV band are summarized in Table 1.

The normalization of the power-law component varied significantly among the different flux states, while that of the reflection continuum remains nearly constant. Thus the two-component model consisting of a variable power law and constant reflection continuum represents the apparent change of the spectral slope in the hard band. The extrapolation of the best-fit model towards lower energies shows significant residuals at energies below 3.5 keV suggesting the presence of absorption, which is explored in subsequent analyses below. An emission line feature is seen at around 6.4 keV. This line was modeled with a Gaussian, and the best-fit parameters are also shown in Table 1. The best-fit Gaussian energy centroid indicates that the line is identified with a K-shell line from neutral or weakly-ionized Fe. The normalization of this component remains constant within errors between the various flux states. The width of this line is relatively narrow: it is consistent with zero width for all the spectra.

A line-like absorption feature is seen around 7 keV in the averaged spectrum and the spectrum in the low-flux

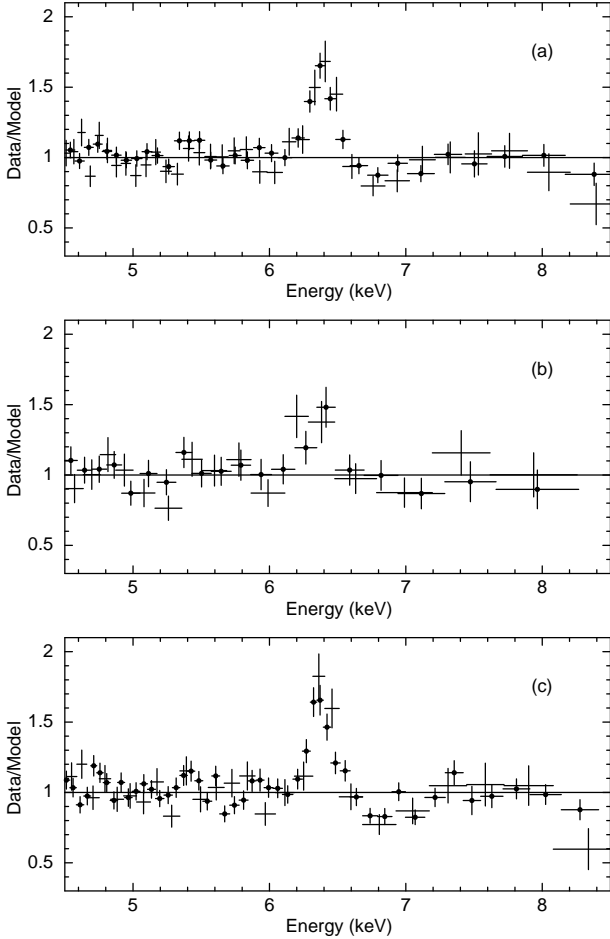


**Fig. 9.** The data/continuum model ratio around the Fe-K emission line in the averaged (a), high flux (b), and low flux (c) spectra. XIS-FI (crosses with filled circles) and XIS-BI (crosses without circles) data are shown. The continuum is the best-fit empirical two-component model fitted in 3.5–40 keV, as shown in Section 4.2.

state. A Gaussian component with a negative normalization was added to represent this feature. The Gaussian width was fixed at  $\sigma = 10$  eV. The result of this fit is also shown in Table 1. The Gaussian energy,  $6.82^{+0.06}_{-0.10}$  keV for the averaged spectrum and  $6.80 \pm 0.04$  keV for the spectrum in the low flux state, is consistent with an absorption line by He-like Fe if an outflow velocity of  $\sim 4600$  km s $^{-1}$  is assumed. A hint of an additional absorption line is present in the spectrum in the low-flux state. When a narrow Gaussian component was added, the value of  $\chi^2$  was reduced by  $\Delta\chi^2 = -10.2$  for two additional parameters (centroid energy and normalization). The line energy,  $7.10^{+0.05}_{-0.06}$  keV, is identified with H-like Fe with an outflow velocity of  $\sim 6000$  km s $^{-1}$  or a He-like resonance line with an outflow velocity of  $\sim 17000$  km s $^{-1}$ . Since the line centroid energy, 7.10 keV, coincided with the energy of the absorption edge for neutral Fe, we examined whether this feature is truly an absorption line or an artifact caused by improper modeling of an Fe edge absorbing the continuum. We used an edge model instead of a Gaussian in

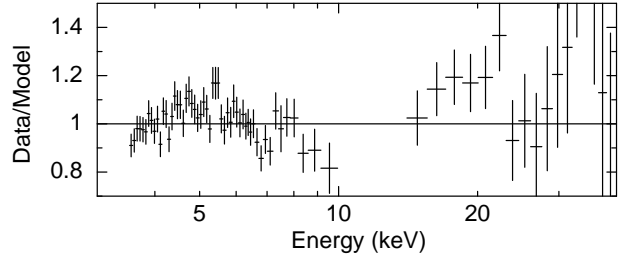


**Fig. 10.** Data/model ratio for a partial-covering model fit to the time-averaged spectrum over the 3.5–4- keV band. The continuum is modeled using a PEXRAV component with the reflection strength fixed at  $R=1$ . For clarity, XIS 1 data are not plotted.

absorption; the edge energy was fixed at 7.1 keV in the source rest frame. The improvement of  $\chi^2$  by adding an edge was  $\Delta\chi^2 = -4.1$ , and we obtained a slightly worse value of  $\chi^2$ , 146.9, compared to the Gaussian case. We also tried to change the Fe abundance in the reflection model instead of introducing a Gaussian or an edge. The best-fit abundance was  $1.35^{+0.30}_{-0.28}$ , with an improvement of  $\Delta\chi^2 = -4.8$ . Thus if there is an additional edge, the significance of the 7.1 keV line becomes weak.

An Fe-K $\beta$  line (7.06 keV in the source rest frame, or 7.04 keV in the observed frame) is not clearly seen in the spectra. This is probably due to the presence of absorption lines around the energy of the Fe-K $\beta$  line. The spectra in the Fe-K bandpass are shown in Fig. 9, where the normalizations of the Gaussians are set to zero.

In the empirical two-component model, the reflection component significantly contributes to the hard X-ray flux, and estimation of the strength of the reflection is affected by the uncertainties in the estimation of the NXB of the HXD PIN. We examined the effect of the uncertainties in the following way. We increased or decreased the level of the NXB by 4%, which is a 90% confidence uncertainty of the NXB estimation for a 40 ksec exposure, and refitted the averaged spectrum with the same model described above. The best-fit  $R$  value is  $R = 7.7$ , while  $R = 9.1$  and  $6.0$  were obtained for the fainter and brighter NXB levels, respectively. The hard X-ray flux is also affected by NXB uncertainties. 15–40 keV fluxes of  $(2.3, 2.0, 2.5) \times 10^{-11}$  erg s $^{-1}$  cm $^{-2}$  were obtained for the nominal, decreased, and increased NXB, respectively.

#### 4.3.2. Complex Absorption Model Fit

Although the empirical model described above represents the observed spectra, physical interpretation of the combination of the very strong reflection continuum and moderate Fe-K emission line ( $R \approx 6.8$  and  $EW \approx 140$  eV for the average spectrum) is not straight-forward, as discussed in Section 5.1. We therefore examined other continuum models for the constant hard spectral component. First we assumed that the intrinsic continuum contains a reflection component of  $R = 1$ , and that the apparent hard spectrum is due to a partial covering absorber. We fitted the averaged spectrum with this partial covering model in the 3.5–40 keV band. The PEXRAV component with

fixed parameters  $\Gamma = 2.04$  and  $R = 1$  was used as a continuum and partial covering absorption was applied. The other PEXRAV parameters, except for the normalization, were fixed to the values shown in the previous subsection. This model is expressed as

$$I(E) = e^{-\sigma(E)N_{\text{H,Gal}}} \{ e^{-\sigma(E)N_{\text{H},1}} f + (1-f) \} \{ AC(E) + G_{\text{Fe}}(E) \},$$

where  $\sigma(E)$ ,  $N_{\text{H,Gal}}$ ,  $N_{\text{H},1}$ ,  $f$ ,  $A$ ,  $C(E)$ , and  $G_{\text{Fe}}(E)$  are the cross section of photoelectric absorption, column density of the Galactic absorption, column density of the intrinsic absorber, covering fraction, normalization factor of the continuum, continuum model, and Gaussians to represent Fe-K emission and absorption lines, respectively. According to this model, the very hard continuum is produced by a partially covered continuum and the leaked emission dilutes the continuum around the Fe-K line to reduce the apparent equivalent width. Although the equivalent width (140 eV) obtained in this fit and the assumed strength of the reflection component ( $R = 1$ ) are consistent with each other, this model resulted in systematic convex residuals in 3.5–7 keV (see Fig. 10). The absorption column density and covering fraction obtained are  $\sim 8.5 \times 10^{23} \text{ cm}^{-2}$  and  $\sim 0.67$ , respectively. The reduced  $\chi^2$  for this model is 1.66 for 124 degrees of freedom (dof) for the averaged spectrum. We added an additional absorbed component to explain the convex residuals:

$$I(E) = e^{-\sigma(E)N_{\text{H,Gal}}} \{ e^{-\sigma(E)N_{\text{H},1}} f AC(E) + (1-f) AC(E) + e^{-\sigma(E)N_{\text{H},2}} BC(E) + G_{\text{Fe}}(E) \},$$

where  $N_{\text{H},2}$  is the column density of the second absorber and  $B$  is the normalization of the additional continuum. This model gave a good fit to the averaged spectrum ( $\chi^2_\nu = 1.10$  for 122 dof). The best-fit column densities and covering fraction are  $N_{\text{H},1} = 2.1 \times 10^{24} \text{ cm}^{-2}$ ,  $N_{\text{H},2} = 5.2 \times 10^{22} \text{ cm}^{-2}$ , and  $f = 0.91$ , respectively. The ratio of the continuum normalizations is  $A/B \approx 2.2$ . Although this model explains the spectral shape in 3.5–40 keV, there are a few problems, as discussed in Section 5.1.

If the small amplitude variability of the hard emission is due to the significant contribution of a reflection component, we need a self-consistent model explaining the strong reflection and the strength of the Fe-K line. One possible idea is that the *EW* of the Fe-K line is apparently small because of complex absorption. Hence we assumed that a reflection continuum and an Fe-K line are partially absorbed by cold material and that the *EW* of the line is 1.0 keV with respect to the reflection continuum. Note that an *EW* of  $\sim 1$  keV is expected for a reflection dominated spectrum (Guainazzi et al. 1998, 2005; Bassani et al. 1999, Levenson et al. 2006). In this model, a PEXRAV component with `rel_refl` = -1 was used for the reflection component, and other parameters in PEXRAV were treated as in Section 4.1. A power law with a fixed photon index of 2.04 was also added to these components. This model explains the average spectrum very well, but

failed to reproduce the shape of the low flux state spectrum, namely the overall flat spectrum and the convex shape in the 3.5–7 keV range. Such a spectral shape is not obtained using this model even if a flatter photon index is allowed. If the power-law component is also partially covered by absorber with distinct parameters (covering fraction and column density), then the spectral shape is explained. This model is expressed using the following equation:

$$I(E) = e^{-\sigma(E)N_{\text{H,Gal}}} \{ e^{-\sigma(E)N_{\text{H},1}} f_1 + (1-f_1) \} \{ AC(E) \} + \{ e^{-\sigma(E)N_{\text{H},2}} f_2 + (1-f_2) \} \{ BR(E) + G_{\text{Fe}}(E) \},$$

where  $C(E)$  is a power-law continuum,  $f$  and  $N_{\text{H}}$  are the covering fraction and column density of the partial absorber, and the subscripts 1 and 2 denote the absorber for the power-law and reflection components, respectively.  $A$  and  $B$  are the normalizations of the power-law and reflection component, respectively, and  $G_{\text{Fe}}(E)$  is Gaussians to represent the Fe-K emission and absorption lines. This model (hereafter referred to as Model-B1) is explored more quantitatively using the full energy band in the next subsection.

#### 4.4. Full-band Spectra

If we extrapolate the best-fit model (Model-A1 or Model-B1) obtained in the previous subsection, the data points are located below the model in the 0.7–3.5 keV band and indicate the presence of a complex absorber and an additional continuum component. The small separation between the data and model at energies below 0.7 keV suggests that the absorber is ionized and that there is an additional soft emission component. The spectra also show absorption features due to ionized O, Ne, and Mg in the 0.5–1.5 keV band, and due to Fe around 7 keV. Such features are indicative of the presence of a multi-zone ionized absorber. We therefore added two ionized absorber components and a blackbody (BB) to model the soft band spectra. We made a grid of ionized absorption usable in XSPEC by using XSTAR in the HEASOFT6.4.1 package. This model assumed a turbulent velocity of  $\sigma = 200 \text{ km s}^{-1}$ , an ionizing continuum with a photon index of 2.0, and solar abundances as in Grevesse & Sauval (1998). The blackbody component was introduced as an empirical representation of the soft excess continuum. We fixed its temperature at  $kT = 0.12 \text{ keV}$ , which is typical of blackbody temperatures measured in Seyfert 1 galaxies (Pounds et al. 2004). Two baseline continuum models, the models A1 and B1 in the previous section, were used. The photon index was fixed at 2.04 unless otherwise noted. Since several narrow emission line features are present, we added Gaussian components to represent them. The widths of the Gaussians were fixed at  $\sigma = 10 \text{ eV}$  unless otherwise noted, while the width of the Fe-K line was left free.

As noted above, an Fe-K $\beta$  emission line is not clearly seen in the spectra. If an Fe-K $\beta$  line at 7.06 keV (source rest frame) was added to the model with an intensity set to 0.13 times that of the Fe-K $\alpha$  line (Palmeri et al. 2003), significant line-like residuals remained around 7.0 keV, suggesting the presence of absorption around this energy due

to highly-ionized Fe. We therefore allowed the redshift parameter for the more highly-ionized absorbing component to vary, and obtained a good fit if the absorption lines are allowed to be blueshifted. After fixing the blueshift of the highly ionized absorber at the best-fit values, this allowed us to then add a Fe-K $\beta$  line with a normalization set to 0.13 times that of the Fe-K $\alpha$  line.

We fitted the three spectra (average, high flux, and low flux) with Models A1 and B1 combined with the ionized absorbers, the BB, and the Gaussians (henceforth referred to as Model-A2 and Model-B2, respectively). Although Model-A2 is probably physically unreasonable, we examined this model first because the number of model parameters is smaller than the other complex models, and the parameters for discrete features are reasonably well-constrained. Model-A2 provided a good fit to the averaged spectra. The best-fit parameters are summarized in Table 2. The possible identifications of the emission lines are also shown in Table 2. Fitting the low flux spectrum with this model resulted in convex residuals in 2–6 keV, which suggests the presence of an additional highly absorbed component. We therefore added an absorbed power-law component with a fixed photon index of 2.04. This model yielded a good fit, as summarized in Table 2. Alternatively, we examined a broad relativistic Fe-K line, instead of the absorbed component, as a possible explanation for the curved spectral shape in the 2–6 keV band. The LAOR line model in XSPEC (Laor 1991) was used for the broad Fe-K line and we fixed the line energy, inner radius, outer radius, emissivity index  $q$  (where the emissivity  $\propto r^q$ ), and inclination at 6.4 keV (source rest frame),  $1.235R_g$ ,  $50R_g$ ,  $-3$ , and  $30^\circ$ , respectively, where  $R_g$  is the gravitational radius,  $GM_{\text{BH}}/c^2$ . This model failed to explain the spectrum ( $\chi^2/\text{dof} = 668/427$ ) and systematic convex residuals remained in the 3–6 keV band. The best-fit equivalent width of the broad and narrow lines were 120 and 140 eV, respectively, which are too small given the strong reflection ( $R \sim 7$ ) for this model.

Next, we examined Model-B2, expressed in the following form:

$$I(E) = e^{-\sigma(E)N_{\text{H,Gal}}} \text{IA}_1(\xi_1, N_{\text{H1}}) \text{IA}_2(\xi_2, N_{\text{H2}}) \\ \times [\{e^{-\sigma(E)N_{\text{H,1}}} f_1 + (1 - f_1)\} \{AC(E) + G(E)\} \\ + \{e^{-\sigma(E)N_{\text{H,2}}} f_2 + (1 - f_2)\} \{BR(E) + G_{\text{Fe}}(E)\}],$$

where  $\text{IA}_1$  and  $\text{IA}_2$  are ionized absorbers,  $G(E)$  is a combination of Gaussians peaking at several different energies, and  $G_{\text{Fe}}(E)$  is two Gaussians to represent the Fe-K $\alpha$  and K $\beta$  emission lines. The parameters of the warm absorbers include the ionization parameter  $\xi \equiv L/nr^2$  (where  $L$  is the isotropic, ionizing luminosity in the 1–1000 ryd range,  $n$  is the electron number density, and  $r$  is the distance from the central continuum source to the absorbing gas), the column density, and the redshift  $z$ . Other components are the same as in Model-B1 in the previous subsection. The  $EW$  of the Fe-K line with respect to the reflection continuum is assumed to be 1.0 keV. We fitted the three spectra with this model (Model-B2) and obtained good fits to the spectra. The best-fit parameters are shown in Table 3.

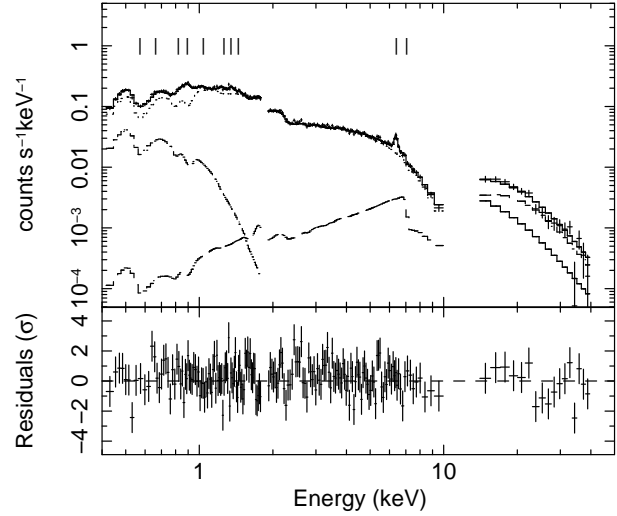


**Fig. 11.** The averaged spectrum fitted with the complex absorber model in the 0.4–40 keV band. Crosses denote the data and the solid histogram denotes the best-fit model. Dotted, dot-dashed, and dashed lines denote the partially covered power-law component, the blackbody component, and partially covered reflection, respectively, with all components modified by ionized absorbers. The best-fit energies of Gaussian components are marked. The lower-panel shows the residuals.

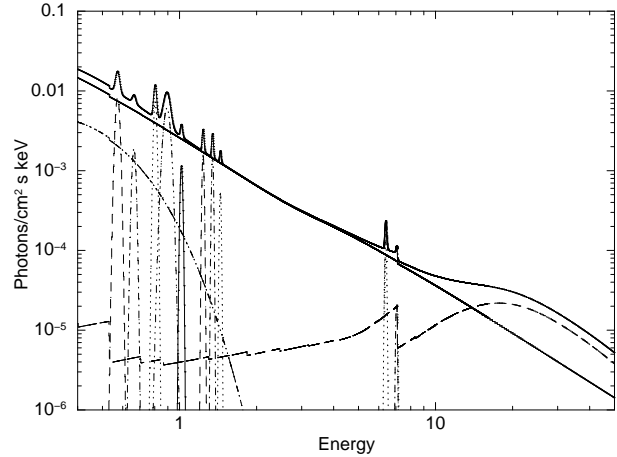


**Fig. 12.** The best-fit model components to the averaged spectrum shown in Fig. 11. The ionized absorbers are removed. The normalization of the models in the energy band of the HXD/PIN is set to unity to connect the model lines in the low and high energy bands for the purpose of presentation.

The best-fit spectrum and incident model spectrum for the averaged spectrum are shown in Fig. 11 and Fig. 12, respectively. The best-fit spectra and incident model spectra for the high and low fluxes are displayed in Figs. 13, 14, 15, and 16, respectively. X-ray fluxes in the 0.5–2, 2–10, and 15–40 keV bands for the best-fit model are listed in Table 4.

In the spectral fits shown above, the power law photon index and the temperature of the blackbody components were fixed at 2.04 and 0.12 keV, respectively. We al-

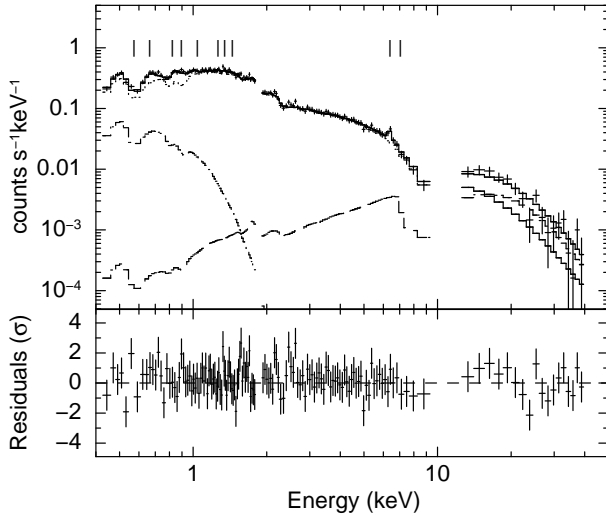


**Fig. 13.** The spectrum in the high flux state fitted with the complex absorber model in the 0.4–40 keV band. The lower-panel shows the residuals. Symbols are same as in Fig. 11.

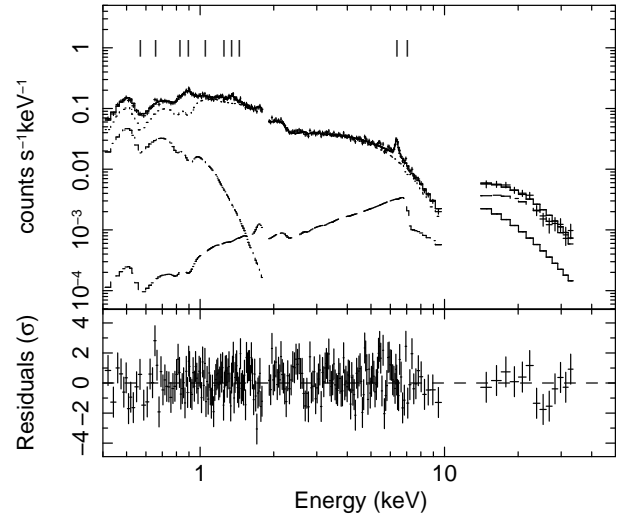


**Fig. 15.** The spectrum in the low flux state fitted with the complex absorber model in the 0.4–40 keV band. The lower-panel shows the residuals. Symbols are same as in Fig. 11.

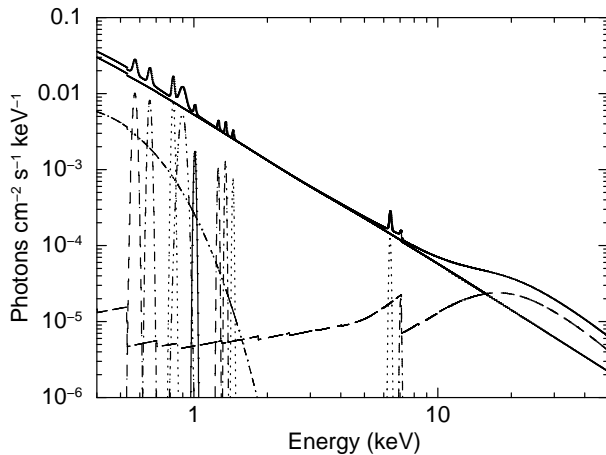


**Fig. 14.** The best-fit model components to the spectrum in the high flux state shown in Fig. 13. The ionized absorbers are removed. The normalization of the models in the energy band of the HXD/PIN is set to unity to connect the model lines in the low and high energy bands for the purpose of presentation.

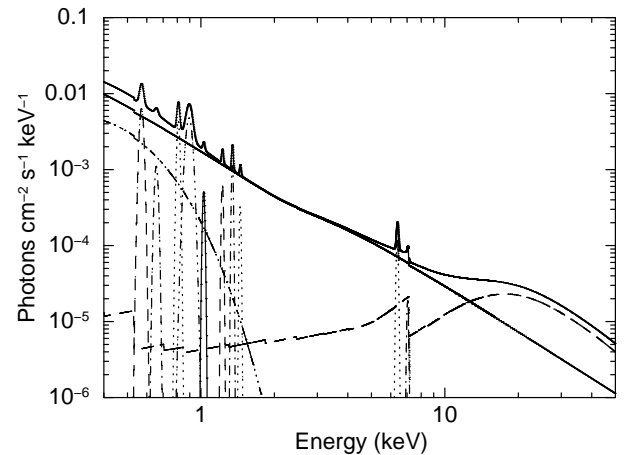


**Fig. 16.** The best-fit model components to the spectrum in the low flux state shown in Fig. 15. The ionized absorbers are removed. The normalization of the models in the energy band of the HXD/PIN is set to unity to connect the model lines in the low and high energy bands for the purpose of presentation.

lowed one of these two parameters to vary to test whether these assumptions are appropriate. We obtained a photon index of  $2.042 \pm 0.008$ ,  $2.041 \pm 0.012$ , and  $2.038^{+0.007}_{-0.008}$  for the averaged, high flux, and low flux spectra, respectively. These results support that the photon index remained almost constant and varied only in its normalization. The temperature of the blackbody component was  $kT = 0.122 \pm 0.005$ ,  $0.121 \pm 0.011$ , and  $0.1176 \pm 0.0004$  keV, for the averaged, high flux, and low flux spectra, respectively. Thus  $kT$  also remained nearly constant.

## 5. Discussion

### 5.1. Two-component Behavior of Spectral Variability

NGC 4051 showed significant spectral variability during our *Suzaku* observation. The spectrum hardens when the source becomes faint and the amplitude of variability is smaller towards higher X-ray energies. This trend of variability is similar to that observed in this object and many other AGNs. Our time-resolved broad-band spectra showed a similar trend at high energies ( $>2$  keV), and can be used to distinguish among various possibilities for the origin of the spectral variability.

#### 5.1.1. The Variable Power-law Component

The spectral variability observed at energies above  $\sim 3.5$  keV is well explained by the two-component model con-

sisting of a variable power-law component and a nearly constant hard component. We modeled the hard component by a reflection continuum (Model-A1, A2) or a partially covered power law plus a partially covered reflection continuum (Model-B1, B2). The photon indices of the power-law component for the difference spectrum, and spectra in the high and low flux states agree with each other ( $\Gamma \approx 2.04$ ). This means that only the normalization of the power-law component varied and that the photon index remained almost constant. Such a model of variability was suggested by Ponti et al. (2006) based on *XMM-Newton* observations of NGC 4051. Similar variability has been observed in MCG-6-30-15 (Miniutti et al. 2007), MCG-5-23-16 (Reeves et al. 2007), etc. This behavior is also consistent with the linear shape of the flux-flux plots in the hard energy bands (Fig. 4(b) and (c)). Therefore, at least in our observation, spectral pivoting (variation in the photon index) is unlikely as the origin of the spectral variability.

#### 5.1.2. The Constant Hard Component

The spectral shape of the constant hard component can be fitted by different models. We first tried to model this component as a continuum consisting of reflection off of cold matter (models A-1 and A-2). This model resulted in very strong reflection ( $R \approx 7$  for the averaged spectrum). A strong reflection with  $R > 1$  could be explained in terms of the effect of light travel time. If the reflector is located far from the nuclear X-ray source, and if the source becomes faint compared to the historical average luminosity,  $R$  can be large. A problem in this model is that the  $EW$  of the Fe-K line is not compatible with the large value of  $R$ . If the geometry of the reflector is assumed to be a cold infinite slab, i.e.,  $R = 1$ , the  $EW$  for the Fe-K fluorescent line is expected to be 100–150 eV, unless the viewing angle is almost edge-on (George & Fabian 1991). The observed  $EW$  should be  $R = 7$  times these expected  $EW$  values, while the observed value is  $EW \approx 140$  eV. Thus the interpretation that the constant component is purely from a reflected continuum is unlikely. A component with a convex shape seen in the low flux state is an additional piece of evidence that the shape of the constant component is not a simple reflection continuum.

In order to solve the apparent inconsistency between the strength of reflection  $R$  and the Fe line  $EW$ , we examined a partial covering model with the PEXRAV component having  $R$  fixed at 1. This model failed to explain the spectrum, and an additional component, an absorbed power law, was required. This model, however, also has difficulties. First, if the best-fit model is extrapolated to lower energies, a very strong excess is seen below 3 keV, which is unusual for spectra of Seyfert galaxies. Secondly, if this idea is correct, X-rays at higher energies must be less-absorbed intrinsic emission. Then it is required that the X-ray source show intrinsic variability with small amplitude and that the observed variability at lower energies is produced mostly by the behavior of the complex absorber. Such intrinsic variability with small amplitude is inconsistent with the trend that AGNs with relatively smaller central black hole masses show more rapid and

larger amplitude variability (e.g., O’Neill et al. 2005).

We assumed that the small amplitude variability at higher energies is due to a significant contribution from reflected emission from matter distant from the nuclear X-ray source. In order to reconcile the strength of the reflection component with the Fe-K  $EW$ , we introduced a partial covering absorber to a combination of reflection and Fe emission. The  $EW$  of the Fe line with respect to the pure reflection continuum is assumed to be 1 keV. This model explains the observed spectra if the power-law emission is also absorbed by a partial coverer, which has parameters distinct from those for the reflection+Fe component (Model-B1, B2). The resulting  $R$  values (the relative strength of the reflection continuum with respect to the power-law component) are 4.3, 2.9, and 5.7 for the averaged, high flux, and low flux spectra, respectively. These numbers are still very large compared to the value expected for a reflector covering a solid angle of  $2\pi$  viewed from the central X-ray source ( $R = 1$ ). Such strong reflection could be due to an effect of light travel time. The observed flux in the 2–10 keV band  $8.1 \times 10^{-12}$  erg s $^{-1}$  cm $^{-2}$  is factor of  $\sim 4$  lower than the flux averaged over 8 yrs, as obtained with *RXTE* PCA ( $\sim 3 \times 10^{-11}$  erg s $^{-1}$  cm $^{-2}$ ) (McHardy et al. 2004). The observed  $R$  value is consistent with this decline of the nuclear flux, if the reflector is located at several light years from the nucleus. The origin of the reflector could be identified with the inner wall of a putative obscuring torus. In this interpretation, the reflected continuum is partially covered by a cold absorber. If the absorbing matter in a torus is patchy, such a partial coverer might be explained. The normalization and the covering fraction of the reflection component remained constant. This fact is consistent with the two-component picture consisting of a variable power-law component and a constant hard component, where the latter is the partially covered reflection component.

The power-law component is also assumed to be partially covered in our model. The power law emission is most likely emitted from the inner region of the accretion disk, and the size of the emitting region could be much smaller than the patchy clouds in a torus. The partial coverer responsible for the power-law component should consist of clouds with a size smaller than the emitting region. A candidate for such clouds is high density, low ionization clumps in a accretion disk wind, which could be identified with ionized absorbers. Although we assumed this absorber is neutral in the spectral fits, a weakly ionized absorber can also explain the spectrum. A spectral component with a convex shape represented by a power law partially absorbed by a column of gas with  $N_H \sim 10^{23}$  cm $^{-2}$  is occasionally observed in Seyfert 1s when the source flux becomes low (NGC 3227, George et al. 1998; Mrk 335, Grupe et al. 2007, 2008) and a similar process could be at work in NGC 4051.

#### 5.1.3. Long-Term Variability of the Hard X-ray Continuum and the Fe-K Emission Line

If the Fe-K emission and reflection continuum are mainly emitted from matter distant from the nucleus, their strengths are expected to be constant over time

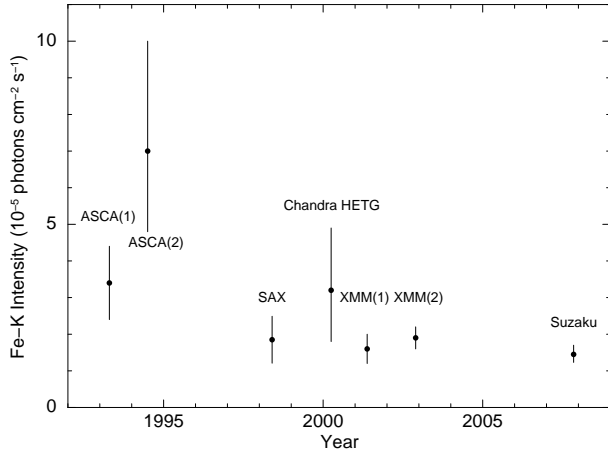


**Fig. 17.** History of Fe-K line intensity. Data are taken from Leighly (1999), Lamer et al. (2003), Yaqoob & Padmanabhan (2004), Pounds et al. (2003), and this work for *ASCA*, *BeppoSAX*, *Chandra* HETG, *XMM-Newton* PN, and *Suzaku*, respectively.

scales of years. Fig. 17 summarizes the observed Fe-K line intensities obtained from past observations. Data from detectors with a moderate or good spectral resolution are shown. The errors correspond to the interval  $\Delta\chi^2 = 2.7$  except for the *BeppoSAX* data point by Lamer et al. (2003), given at a  $1\sigma$  level. The Fe-K line intensities are nearly constant over 10 years and consistent with the idea that a significant fraction of the Fe-K line is emitted from distant matter. The second *ASCA* data point shows a larger error than others. In this fit, the line was broad ( $\sigma = 0.5$  keV) (Leighly 1999). A possible interpretation is that a broad Fe-K component originating from the inner part of accretion disk contributes to the flux and/or that uncertainties in continuum modeling artificially make the line seem broader and stronger.

If reflected emission makes a significant contribution to the hard X-ray band as we have measured, hard X-ray fluxes are also expected to remain nearly constant. The history of hard X-ray fluxes is summarized in Table 5. We calculated hard X-ray fluxes in various energy bands by using our averaged *Suzaku* spectrum and the best-fit complex absorption model (Model-B2), and compared with published hard X-ray measurements. The variations in hard X-ray fluxes among *INTEGRAL*, *Swift*, and *Suzaku* observations are less than  $\sim 50\%$ , although assumptions on the spectral shape and cross calibration between the instruments introduce large uncertainties. For example, Beckmann et al. (2006) measured a photon index of  $\Gamma = 2.62$  in the hard X-ray band with *INTEGRAL* ISGRI. This index is incompatible with the *Suzaku* PIN data, which gives  $\Gamma = 1.46^{+0.31}_{-0.22}$  if a simple power law is assumed. If  $\Gamma = 2.62$  was assumed to fit the *Suzaku* PIN spectrum, reduced  $\chi^2 = 3.8$  (16 dof) and a 20–40 keV flux of  $1.1 \times 10^{-11}$  erg s<sup>-1</sup> cm<sup>-2</sup>, which is about 60% lower than the value for the best-fit model, were obtained. Thus we conclude that hard X-ray fluxes did not significantly change among *INTEGRAL*, *Swift*, and *Suzaku* measure-

ments.

The hard X-ray flux obtained with *BeppoSAX* is  $7.9 \times 10^{-12}$  erg s<sup>-1</sup> cm<sup>-2</sup> in the 15–40 keV band if the model given in Guainazzi et al. (1998) is assumed. This flux is about a factor of 3 lower than that obtained with *Suzaku* ( $2.4 \times 10^{-11}$  erg s<sup>-1</sup> cm<sup>-2</sup>). The *BeppoSAX* observation was done when the source was in a ultra-dim state and the direct power-law component could have been switched off. If we set the normalization of the power-law component to zero in our *Suzaku* spectrum, the 15–40 keV flux becomes  $1.8 \times 10^{-11}$  erg s<sup>-1</sup> cm<sup>-2</sup>. Although this value is still about a factor of 2 larger than the *BeppoSAX* value, we consider the change between the two observations to not be significant since the error bars at high energies in the spectrum obtained with the PSD are relatively large.

The width of the Fe-K fluorescent line is expected to be narrow if the reflector is located far from the nucleus. The line width we obtained is consistent with being narrow and agrees with the idea that the contribution from distant matter is significant. The line width measured with *Chandra* HETG is  $6330^{+1311}_{-4550}$  km s<sup>-1</sup> at the 90% confidence level for three parameters of interest (Yaqoob & Padmanabhan 2004). The lower bound of the error range is larger than the width of the optical or UV broad lines ( $1110 \pm 190$  km s<sup>-1</sup> for variable broad H $\beta$  and  $1040 \pm 250$  km s<sup>-1</sup> for CIV $\lambda$ 1549; Peterson et al. 2000, Collinge et al. 2001). The line profile shows a prominent narrow core and a broad residuals in 5–6.4 keV (Fig. 4 in Yaqoob & Padmanabhan 2004). The combination of these two components presumably resulted in the very large error range, and a narrower core width would be allowed if a better quality high-resolution spectrum is used to distinguish multiple components.

## 5.2. The Effect of Absorption

The difference spectrum above 3.5 keV is fitted with a pure power-law component, while the low energy part of the data shows a large deficit when the power law is extrapolated from higher energies. The hard X-ray spectrum in the low flux state shows a component with a convex shape, represented by a partial covering model (Model-B2). These facts suggest that variability of the absorbing components is another important factor in the spectral variability. In Model-B2, the power-law continuum is covered by gas with a column density of  $N_H \sim 1 \times 10^{23}$  cm<sup>-2</sup>, and its covering factor varies with the flux. This change explains most of the spectral variability below 3.5 keV. In fact, if the normalization of the power-law component is increased and the covering fraction is decreased in the best-fit model for the low flux, the broad band continuum shape in the high flux state is mostly recovered. Weak positive residuals are seen around 0.65–0.7 keV and 1.2–1.8 keV, which may be related to small changes of ionized absorbers. Most of the the Gaussian emission lines did not show significant variability, and the equivalent widths were larger in the low flux state. These results and the RMS spectra showing smaller amplitudes at energies of several emission lines imply that a significant fraction of the emission line fluxes originate in an ex-

tended region, likely photo-ionized by the emission from the central source. The low flux state observed in 2002 with *XMM-Newton* also showed emission lines (Pounds et al. 2003, Uttley et al. 2004, Ponti et al. 2006), which are also compatible with the extended plasma origin of the lines.

Fig. 18 shows that the change of the power-law normalization and the covering fraction can explain the most of the spectral variability observed between the high and low flux states. In the following procedure, only continuum components are considered. We first changed the normalization of the power-law component in the best-fit model in the high flux state, setting it to the best-fit normalization for the low flux state. This model was then divided by the best-fit model for the high flux state. This ratio is shown as a dashed line in Fig. 18. The ratio between the best-fit models in the low and high flux states are shown as a solid line in Fig. 18. The comparison between these two lines shows that the spectral variability above 5 keV is mostly explained by changing only the power-law normalization. Next, we set both the normalization and the covering factor for the power-law component at the best-fit values in the low flux state, and divided this model by the best-fit model for the high flux state. This ratio is shown as a dot-dashed line in Fig. 18, and it almost reproduces the spectral shape in the low flux state. Thus we conclude that the main causes of the spectral variability are variations in the normalization of the power-law component with a constant photon index, and variations in the covering fraction of the absorber, which is assumed to be neutral in the fit and could be weakly ionized. Additional contributors to the observed spectral variability include small-amplitude changes of the warm absorbers and the normalization of the BB component.

## 6. Summary and Conclusions

We analyzed data from a *Suzaku* observation of NGC 4051 obtained in 2005 Nov. and studied broadband spectral variability. The averaged 2–10 keV flux was  $8.1 \times 10^{-12} \text{ erg s}^{-1} \text{ cm}^{-2}$ , which is several times lower than the historical average ( $\sim 3 \times 10^{-11} \text{ erg s}^{-1} \text{ cm}^{-2}$ ) and larger than the lowest flux observed in 1998 ( $1.3 \times 10^{-12} \text{ erg s}^{-1} \text{ cm}^{-2}$ ). NGC 4051 showed large amplitude variability during our observation. Several flare-like increases in the X-ray flux were observed. The spectra became flatter when the source flux was low. We examined the averaged spectrum and spectra in high and low flux time intervals and identified variable components.

The difference spectrum in the 3.5–40 keV band is well fitted by a power-law component with a photon index of 2.04. This photon index is in agreement with those measured for the high/low flux spectra, and suggests that variations in the normalization of a power law with a constant photon index combined with a nearly constant hard component is the primary cause of the spectral variability above 3.5 keV.

We fitted the full-band spectra with a model consisting of a power law, reflection continuum from cold matter, a

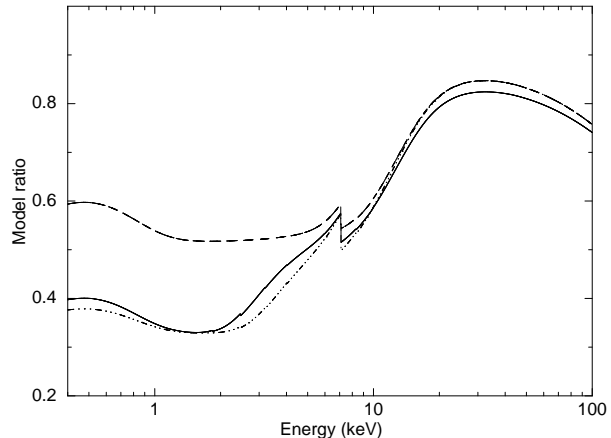


**Fig. 18.** Contribution of the change of the power-law component to the spectral variability. Solid line: Ratio between the best-fit models in the low and high flux states. Dashed-line: The best-fit model in the high flux state with the best-fit power-law normalization in the low flux state, divided by the best-fit model in the high flux state. Dot-dot-dot-dashed line: The best-fit model in the high flux state with the best-fit power-law normalization and covering fraction in the low flux state, divided by the best-fit model in the high flux state.

blackbody, two zones of ionized absorbing material, and several Gaussian emission lines. The hard constant component is dominated by a reflection continuum originating in cold matter (Model-A2), the amount of reflection was  $R \sim 7$  for the averaged spectrum, where  $R = 1$  corresponds to the situation that the infinite slab subtends a solid angle of  $2\pi$  as viewed from the illuminating source, and we assumed an inclination angle of  $45^\circ$ . The observed *EW* of the Fe-K line (140 eV), however, is too small for the strong reflection. The hard constant component therefore cannot be explained only by a reflection continuum component. We adopted a combination of partially covered reflection and partially covered power-law emission as a model for the hard component, and successfully explained the amount of reflection, the Fe line *EW*, and the variability of the overall spectral shape. In this model, an additional cause of spectral variability is the change of the covering factor for the power-law component. The large covering fraction of the power-law component is justified by the spectral shape in the low flux state, which shows a convex shape reminiscent of a spectrum absorbed by  $\sim 1 \times 10^{23} \text{ cm}^{-2}$ . The large amount of reflection is presumably due to a light travel time effect, since the flux in our observation is a factor of  $\sim 4$  lower than the historically averaged flux. The parameters for the ionized absorbers, blackbody, and Gaussian emission lines were nearly constant, and their contribution to spectral variability is very limited. The constant emission line intensities are consistent with an origin in extended, ionized gas.

In summary, we identified the causes of spectral variability as follows. At high energies ( $>3.5 \text{ keV}$ ) the primary cause of the spectral variability is variations in the nor-

malization of the power-law component with a constant photon index ( $\Gamma=2.04$ ) overlaid on a nearly constant hard component. The constant hard component is interpreted as a partially covered continuum. At lower energies, variations in the covering fraction of the gas absorbing the power-law continuum is an additional cause of the spectral variability. Variations in the warm absorber parameters and the normalization of the blackbody component do not significantly contribute to the spectral variability.

We thank an anonymous referee for useful comments that improved the manuscript. We are grateful to all the members of the *Suzaku* team. The authors thank T. Kallman for writing and supporting the XSTAR software. This work is partially supported by Grants-in-Aid for Scientific Research (20740109).

## References

- Arévalo, P., McHardy, I. M., Markowitz, A., Papadakis, I. E., Turner, T. J., Miller, L., & Reeves, J. N. 2008, *MNRAS*, 387, 279
- Awaki, H., Koyama, K., Inoue, H., & Halpern, J. P. 1991, *PASJ*, 43, 195
- Bassani, L., et al. 1999, *ApJS*, 121, 473
- Beckmann, V., Gehrels, N., Shrader, C. R., & Soldi, S. 2006, *ApJ*, 638, 642
- Boldt, E. 1987, *IAUS*, 124, 611
- Collinge, M. J., et al. 2001, *ApJ*, 557, 2
- Fabian, A. C., Miniutti, G., Gallo, L., Boller, Th., Tanaka, Y., Vaughan, S., & Ross, R. R. 2004, *MNRAS*, 353, 1071
- Gallo, L. C. 2006, *MNRAS*, 368, 479
- Gallo, L. C., Tanaka, Y., Boller, Th., Fabian, A. C., Vaughan, S. M. & Brandt, W. N. 2004, *MNRAS*, 353, 1064
- Gallo, L. C., Boller, Th., Tanaka, Y., Fabian, A. C. Brandt, W. N., Welsh, E. F., Anabuki, N., & Haba, Y. 2007, *MNRAS*, 347, 269
- George, I. M., & Fabian, A. C. 1991, *MNRAS*, 249, 352
- George, I. M., Mushotzky, R. F., Turner, T. J., Yaqoob, T., Ptak, A., Nandra, K., & Netzer, H. 1998, *ApJ*, 509, 146
- Grevesse, N., & Sauval, A. J. 1998, *Space Science Reviews*, 85, 161
- Gruber, D. E., Matteson, J. L., Peterson, L. E., & Jung, G. V. 1999, *ApJ*, 520, 124
- Grupe, D., Komossa, S., & Gallo, L. 2007, *ApJ*, 668, L111
- Grupe, D., et al. 2008, *ApJ*, 681, 982
- Guainazzi, M., et al. 1998, *MNRAS*, 301, L1
- Guainazzi, M., Fabian, A. C., Iwasawa, K., Matt, G., & Fiore, F. 2005, *MNRAS*, 356, 295
- Itoh, T., et al. 2008, *PASJ*, 60, S251
- Kalberla, P. M. W., Burton, W. B., Hartmann, D., Arnal, E. M., Bajaja, E., Morras, R., & Pöppel, W. G., L. 2005, *A&A*, 440, 775
- Koyama, K., et al. 2007, *PASJ*, 59, S23
- Krivonos, R., Revnivtsev, M., Lutovinov, A., Sazonov, S., Churazov, E., & Sunyaev, R. 2007, *A&A*, 475, 775
- Kunieda, H., Hayakawa, S., Tawara, Y., Koyama, K., Tsuruta, S., & Leighly, K. 1992, *ApJ*, 384, 482
- Lamer, G., McHardy, I. M., Uttley, P., & Jahoda, K. 2003, *MNRAS*, 338, 323
- Leighly, K. M. 1999, *ApJS*, 125, 317
- Laor, A. 1991, *ApJ*, 376, 90
- Lawrence, A., Watson, M. G., Pounds, K. A., & Elvis, M. 1985, *MNRAS*, 217, 685
- Levenson, N. A., Heckman, T. M., Krolik, J. H., Weaver, K. A., & Życki, P. T. 2006, *ApJ*, 648, 111
- McHardy, I. M., Papadakis, I. E., Uttley, P., Page, M. J., & Mason, K. O. 2004, *MNRAS*, 348, 783
- Magdziarz, P. & Zdziarski, A. A. 1995, *MNRAS*, 273, 837
- Markowitz, A., Edelson, R., & Vaughan, S. 2003, *ApJ*, 598, 935
- Markowitz, A., & Edelson, R. 2004, *ApJ*, 617, 939
- Matsuoka, M., Piro, L., Yamauchi, M., & Murakami, T. 1990, *ApJ*, 361, 440
- Miniutti, G., et al. 2007, *PASJ*, 59, S315
- Miniutti, G., & Fabian, A. C. 2004, *MNRAS*, 349, 1435
- Mitsuda, K., et al. 2007, *PASJ*, 59, S1
- Mizuno, T., et al. 2007, *JX-ISAS-SUZAKU-MEMO-2006-42*
- O'Neill, P. M., Nandra, K., Papadakis, I. E., & Turner, T. J. 2005, *MNRAS*, 358, 1405
- Palmeri, P., Mendoza, C., Kallman, T. R., Bautista, M. A., & Meléndez, M. A. 2006, *A&A*, 410, 359
- Peterson, B. M., et al. 2000, *ApJ*, 542, 161
- Ponti, G., Miniutti, G., Cappi, M., Maraschi, L., Fabian, A. C., & Iwasawa, K. 2006, *MNRAS*, 368, 903
- Pounds, K. A., Reeves, J. N., King, A. R., & Page, K. L. 2004, *MNRAS*, 350, 10
- Reeves, J., et al. 2007, *PASJ*, 59, S301
- Serlemitsos, P. J., 2007, *PASJ*, 59, S9
- Sazonov, S., Revnivtsev, M., Krivonos, R., Churazov, E., & Sunyaev, R. 2007, *A&A*, 462, 57
- Shirai, H., et al. 2008, *PASJ*, 60, S263
- Takahashi, T., et al. 2007, *PASJ*, 59, S35
- Taylor, R. D., Uttley, P., & McHardy, I. M. 2003, *MNRAS*, 342, L31
- Tueller, J., et al. 2008, *ApJ*, 681, 113
- Uttley, P., McHardy, I. M., Papadakis, I. E., Guainazzi, M., & Fruscione 1999, *MNRAS*, 307, L6
- Uttley, P., Taylor, R. D., McHardy, I. M., Page, M. J., Mason, K. O., Lamer, G., & Fruscione, A. 2004, *MNRAS*, 347, 1345
- Vaughan, S., Edelson, R., Warwick, R. S., & Uttley, P. 2003, *MNRAS*, 345, 1271
- Vaughan, S., & Fabian, A. C. 2004, *MNRAS*, 348, 1415
- Yaqoob, T., & Padmanabhan, U. 2004, *ApJ*, 604, 63

**Table 1.** Spcetral Parameters for Emprical Two Component Model fitted in 3.5–40 keV\*.

Flux State	Average	High Flux	Low Flux
Power law			
Photon index	2.04(f)	2.04(f)	2.04(f)
Normalization <sup>†</sup>	$2.40(2.35 - 2.50) \times 10^{-3}$	$4.73(4.51 - 4.94) \times 10^{-3}$	$1.91(1.84 - 1.98) \times 10^{-3}$
Reflection <sup>‡</sup>			
Normalization <sup>§</sup>	$18.0(17.0 - 19.2) \times 10^{-2}$	$18.4(15.4 - 21.4) \times 10^{-2}$	$18.2(17.2 - 19.1) \times 10^{-2}$
$R^{\parallel}$	7.7	3.88	9.68
Gaussians <sup>#</sup>			
Energy (keV)	6.397(6.382 – 6.412)	6.370(6.308 – 6.426)	6.389(6.375 – –6.403)
Width (keV)	0.044 (0 – 0.075)	0.077 (0 – 0.15)	0.029 (0 – 0.059)
Normalization**	1.45(1.22 – 1.70)	1.92(1.11 – 2.74)	0.126(0.108 – 0.144)
EW (eV)	140(119 – 164)	122(71 – 174)	135(115 – 155)
Energy (keV)	6.82(6.72 – 6.88)	...	6.80(6.76 – 6.84)
Width (keV)	0.01(f)	...	0.01(f)
Normalization	$-0.38(-0.54 - -0.21)$	...	$-0.40(-0.54 - -0.27)$
EW (eV)	$-40(-57 - -22)$	...	$-46(-65 - -33)$
Energy (keV)	...	...	7.10(7.04 – 7.15)
Width (keV)	...	...	0.01(f)
Normalization	...	...	$-0.27(-0.40 - -0.14)$
EW (eV)	...	...	$-40(-59 - -21)$
$\chi^2_{\nu}/\text{dof}$	123.6/122	66.2/72	140.5/116

Notes.

\* (f) denotes fixed parameter. Numbers in parentheses are error ranges for  $\Delta\chi^2 = 2.7$ .† Normalization of power law in units of photons  $\text{keV}^{-1} \text{ cm}^{-2} \text{ s}^{-1}$  at 1 keV in the source rest frame.‡ Inclination angle of  $45^\circ$  was assumed.§ Normalization of reflection continuum in units of photons  $\text{keV}^{-1} \text{ cm}^{-2} \text{ s}^{-1}$  at 1 keV of the incident power law only in the observed frame.

|| Ratio of power law normalization to normaliztion of reflection.

# Gaussian center energies are in the source rest frame.

\*\*  $10^{-5}$  photons  $\text{cm}^{-2} \text{ s}^{-1}$  in the line.

**Table 2.** Spectral Parameters for Empirical Two Component Model\*.

Flux	Average	High Flux	Low Flux	Line ID
Power law + Reflection <sup>†</sup>				
Photon index	2.04(f)	2.04(f)	2.04(f)	
Normalization <sup>‡</sup>	2.66 (2.64–2.68) × 10 <sup>−3</sup>	5.08 (5.02–5.13) × 10 <sup>−3</sup>	1.72 (1.70–1.73) × 10 <sup>−4</sup>	
$R$	6.9 (6.6–7.1)	3.7 (3.2–4.0)	8.7 (8.3–9.0)	
Blackbody				
$kT$ (keV)	0.12(f)	0.12(f)	0.12(f)	
Normalization <sup>§</sup>	1.71 (1.59–1.83) × 10 <sup>−5</sup>	3.50 (3.15–3.92) × 10 <sup>−5</sup>	2.09 (2.01–2.20) × 10 <sup>−5</sup>	
Power law				
Photon index	...	...	2.04(f)	
Normalization <sup>  </sup>	...	...	7.1 (6.7–7.5) × 10 <sup>−4</sup>	
$N_H$ (10 <sup>22</sup> cm <sup>−2</sup> )	...	...	53(47–59)	
Ionized absorber (1) <sup>#</sup>				
$\log \xi$	1.84 (1.83–1.85)	1.76 (1.74–1.78)	1.84 (1.82–1.85)	
$N_H$ (10 <sup>22</sup> cm <sup>−2</sup> )	1.42 (1.23–1.59)	1.60 (1.54–1.68)	1.94 (1.90–2.00)	
Ionized absorber (2) <sup>**</sup>				
$\log \xi$	2.64 (2.63–2.67)	2.89 (2.54–2.94)	2.98 (2.93–3.00)	
$N_H$ (10 <sup>22</sup> cm <sup>−2</sup> )	1.43 (1.26–1.63)	1.5 (1.0–2.3)	2.7 (1.8–3.4)	
Gaussians <sup>††,‡‡</sup>				
Energy (keV)	0.582 (0.577–0.587)	0.577 (0.563–0.589)	0.567 (0.561–0.573)	OVII K $\alpha$
Normalization <sup>§§</sup>	22.7 (19.7–26.5)	23.4 (13.7–32.6)	16.5 (13.4–20.5)	
EW (eV)	22	12	20	
Energy (keV)	0.675 (0.664–0.687)	0.659 (0.650–0.667)	0.653 (0.639–0.666)	OVI Ly $\alpha$
Normalization	7.0 (5.1–8.9)	23 (18–30)	3.4 (1.7–5.0)	
EW (eV)	9	16	6	
Energy (keV)	0.831 (0.824–0.837)	0.827 (0.821–0.833)	0.803 (0.794–0.813)	Fe XVII L?
Normalization	12 (10–14)	20 (16–24)	5.3 (3.6–7.1)	
EW (eV)	23	24	14	
Energy (keV)	...	...	0.884 (0.880–0.887)	Fe XVIII L?
Normalization	...	...	24 (22–25)	
EW (eV)	...	...	66	
Energy (keV)	0.916 (0.914–0.918)	0.898 (0.890–0.910)	0.912 (0.905–0.920)	Ne IX K $\alpha$
Normalization	48 (46–51)	16 (12–19)	8.2 (6.6–9.8)	
EW (eV)	127	22	20	
Energy (keV)	1.037 (1.030–1.042)	...	1.026 (1.006–1.044)	Ne X Ly $\alpha$
Normalization	5.1 (4.4–6.0)	...	0.93 (0.33–1.5)	
EW (eV)	18	...	5	
Energy (keV)	...	...	1.26 (1.24–1.27)	Fe XXIII L?
Normalization	...	...	1.5 (1.0–1.9)	
EW (eV)	...	...	12	
Energy (keV)	1.38 (1.37–1.39)	1.35 (1.30–1.38)	1.35 (1.34–1.36)	MgXI K $\alpha$
Normalization	2.5 (2.1–3.0)	1.9 (0.6–3.3) × 10 <sup>−5</sup>	2.5 (2.1–2.8)	
EW (eV)	17	6	25	
Energy (keV)	1.470 (1.445–1.490)	1.443 (1.416–1.474)	...	Mg XII Ly $\alpha$
Normalization	0.79 (0.38–1.18)	2.4 (1.3–3.6)	...	
EW (eV)	6	10	...	
Energy (keV)	6.534 (6.517–6.550)	6.524 (6.469–6.597)	6.393 (6.379–6.406)	Fe K $\alpha$
Width (keV)	0.035 (0–0.059)	0.080 (0.022–0.156)	0.034 (0.0–0.056)	
Normalization	1.51 (1.30–1.69)	1.98 (1.29–2.67)	1.41 (1.24–1.58)	
EW (eV)	140	119	179	
$\chi^2_\nu$ (dof)	614.0/486	342.8/309	570.1/421	

Notes.

\* (f) denotes fixed parameter. Numbers in parentheses are error ranges for  $\Delta\chi^2 = 2.7$ .

† Inclination angle of 45° was assumed.

‡ Normalization of reflection continuum in units of photons keV<sup>−1</sup> cm<sup>−2</sup> s<sup>−1</sup> at 1 keV of the incident power law only in the observed frame.§ Normalization of Blackbody defined as  $L_{45}/D_{10\text{Mpc}}$ , where  $L_{45}$  is the source luminosity in units of 10<sup>45</sup> erg s<sup>−1</sup> and  $D_{10\text{Mpc}}$  is the distance to the source in units of 10 Mpc.|| Normalization of power law in units of photons keV<sup>−1</sup> cm<sup>−2</sup> s<sup>−1</sup> at 1 keV in the source rest frame.# Redshift parameter for the warm absorber model with a low ionization parameter is fixed at the redshift of NGC 4051 ( $z = 0.002336$ ).\*\* Redshift parameter for the warm absorber model with a high ionization parameter is fixed at the value at the  $\chi^2$  minimum ( $z = -0.0575, -0.059$ , and  $-0.0551$  for average, high flux, and low flux spectra, respectively).

†† Width of the Gaussian at 6.4 keV was left free. Widths of other Gaussians were fixed at 10 eV.

‡‡ Fe K $\beta$  line at 7.06 keV (source rest frame) with a normalization of 0.13 times that of Fe K $\alpha$  line is also added. The width of Fe K $\alpha$  and K $\beta$  lines are assumed to be common.§§ 10<sup>−5</sup> photons cm<sup>−2</sup> s<sup>−1</sup> in the line.

**Table 3.** Spcctral Parameters for Complex Absorber Model\*.

Flux state	Average	High Flux	Low Flux	Line ID
Pratially Covered Power law				
Photon index	2.04(f)	2.04(f)	2.04(f)	
Normalization <sup>†</sup>	4.16 (4.13–4.19)×10 <sup>-3</sup>	6.43 (6.35–6.50)×10 <sup>-3</sup>	3.32 (3.29–3.35)×10 <sup>-3</sup>	
$N_H$ (10 <sup>22</sup> cm <sup>-2</sup> )	11.9 (10.9–13.0)	12.1 (8.6–18.7)	7.7 (7.1–8.2)	
Covering fraction	0.360 (0.349–0.370)	0.156 (0.122–0.187)	0.464 (0.455–0.473)	
Partially Covered Reflection <sup>‡</sup>				
$R$	-1(f)	-1(f)	-1(f)	
Normalization <sup>§</sup>	1.78 (1.68–1.89)×10 <sup>-2</sup>	1.94 (1.65–2.22)×10 <sup>-2</sup>	1.89 (1.79–2.00)×10 <sup>-2</sup>	
$N_H$ (10 <sup>22</sup> cm <sup>-2</sup> )	100(f)	100(f)	100(f)	
Covering fraction	0.806 (0.775–0.834)	0.786 (0.708–0.880)	0.802 (0.776–0.825)	
Blackbody				
$kT$ (keV)	0.12(f)	0.12(f)	0.12(f)	
Normalization <sup>  </sup>	3.26 (3.10–3.49)×10 <sup>-5</sup>	3.53(3.06 – 4.00) × 10 <sup>-5</sup>	4.10 (3.88–4.33)×10 <sup>-5</sup>	
Ionized absorber (1) <sup>#</sup>				
log $\xi$	1.79 (1.78–1.80)	1.79 (1.77–1.81)	1.82 (1.800–1.83)	
$N_H$ (10 <sup>22</sup> cm <sup>-2</sup> )	2.28 (2.23–2.31)	1.90 (1.83–1.97)	2.06 (2.01–2.10)	
Ionized absorber (2) <sup>**</sup>				
log $\xi$	2.96 (2.94–3.00)	2.71 (2.68–2.75)	2.97 (2.91–3.02)	
$N_H$ (10 <sup>22</sup> cm <sup>-2</sup> )	2.74 (2.04–3.5)	1.30 (1.02–1.80)	1.27 (0.87–1.75)	
Gaussians <sup>††,‡‡</sup>				
Energy (keV)	0.572 (0.567–0.5767)	0.574 (0.560–0.587)	0.570 (0.5642–0.576)	OVII K $\alpha$
Normalization <sup>§§</sup>	36.3 (31.2–42.1)	33.2 (21.5–45.3)	33.3 (27.6–39.4)	
EW (eV)	22	14	22	
Energy (keV)	0.664 (0.649–0.679)	0.660 (0.654–0.667)	0.658 (0.639–0.675)	OVI Ly $\alpha$
Normalization	8.1 (5.5–10.8)	2.6 (1.9–3.2)	5.6 (2.6–8.6)	
EW (eV)	7	15	5	
Energy (keV)	0.822 (0.818–0.827)	0.841 (0.8346–0.8463)	0.827 (0.821–0.832)	Fe XVII L?
Normalization	31 (27–34)	26 (20–31)	22 (19–25)	
EW (eV)	38	23	32	
Energy (keV)	0.895 (0.893–0.897)	0.899 (0.892–0.906)	0.896 (0.894–0.899)	Ne IX K $\alpha$
Normalization	63 (60–66)	42 (35–47)	58 (55–61)	
EW (eV)	106	48	117	
Energy (keV)	1.041 (1.027–1.056)	1.032 (0.995–1.050)	1.050 (1.024–1.066)	Ne X LyXS $\alpha$
Normalization	4.7 (3.3–5.8)	5.3 (2.5–7.9)	2.4 (1.4–3.7)	
EW (eV)	11	8	7	
Energy (keV)	1.265 (1.259–1.271)	1.279 (1.253–1.307)	1.253 (1.236–1.265)	Fe XXIII L?
Normalization	6.3 (5.5–7.3)	3.1 (1.4–5.0)	3.0 (2.3–4.0)	
EW (eV)	22	8	13	
Energy (keV)	1.349 (1.342–1.353)	1.351 (1.325–1.363)	1.349 (1.343–1.355)	Mg XI K $\alpha$
Normalization	6.5 (5.5–6.7)	3.9 (2.1–5.7)	5.4 (4.8–6.3)	
EW (eV)	26	11	29	
Energy (keV)	1.447 (1.434–1.463)	1.449 (1.426–1.477)	1.449 (1.430–1.467)	Mg XII Ly $\alpha$
Normalization	2.1 (1.4–2.7)	2.3(0.8–3.7)	1.6 (1.0–2.2)	
EW (eV)	10	7	10	
Energy (keV)	6.400 (6.385–6.414)	6.380 (6.323–6.435)	6.393 (6.380–6.408)	Fe K $\alpha$
Width (keV)	0.0469 (0.018–0.067)	0.052 (0–0.129)	0.056 (0.036–0.077)	
Normalization	4.9	5.2	5.1	
EW (keV) <sup>   </sup>	1.0(f)	1.0(f)	1.0(f)	
$\chi^2_\nu$ (dof)	585.0/480	341.0/302	525.9/420	

Notes.

\* (f) denotes fixed parameter. Numbers in parentheses are error ranges for  $\Delta\chi^2 = 2.7$ .† Normalization of power law in units of photons keV<sup>-1</sup> cm<sup>-2</sup> s<sup>-1</sup> at 1 keV in the source rest frame.

‡ Inclination angle of 45° was assumed.

‡ Normalization of reflection continuum in units of photons keV<sup>-1</sup> cm<sup>-2</sup> s<sup>-1</sup> at 1 keV of the incident power law only in the observed frame.§ Normalization of Blackbody defined as  $L_{45}/D_{10\text{Mpc}}$ , where  $L_{45}$  is the source luminosity in units of 10<sup>45</sup> erg s<sup>-1</sup> and  $D_{10\text{Mpc}}$  is the distance to the source in units of 10 Mpc.|| Redshift parameter for the warm absorber model with a low ionization parameter is fixed at the redshift of NGC 4051 ( $z = 0.002336$ ).# Redshift parameter for the warm absorber model with a high ionization parameter is fixed at the value at the  $\chi^2$  minimum ( $z = -0.061, -0.059$ , and  $-0.049$  for average, high flux, and low flux spectra, respectively).

\*\* Gaussian center energies are in the source rest frame.

†† Width of the Gaussian at 0.89 keV fixed at 25 eV. Width of the Gaussian at 6.4 keV was left free. Widths of other lines were fixed at 10 eV.

‡‡ Fe K $\beta$  line at 7.06 keV (source rest frame) with a normalization of 0.13 times that of Fe K $\alpha$  line was also added. The width of Fe K $\alpha$  and K $\beta$  lines are assumed to be common.§§  $10 \times 10^{-5}$  photons cm<sup>-2</sup> s<sup>-1</sup> in the line.

||| Equivalent width was fixed at 1 keV with respect to the pure reflection continuum before affected by absorption.

**Table 4.** Observed X-ray Fluxes for the Complex Absorber Model

Flux state	Flux (0.5–2 keV) ( $10^{-11}$ erg s $^{-1}$ cm $^{-2}$ )	Flux (2–10 keV) ( $10^{-11}$ erg s $^{-1}$ cm $^{-2}$ )	Flux (15–40 keV) ( $10^{-11}$ erg s $^{-1}$ cm $^{-2}$ )
Average	0.39	0.82	2.4
High flux	0.78	1.4	2.9
Low flux	0.30	0.68	2.3

**Table 5.** Histroy of Hard X-ray Flux

Date	Instrument	Flux ( $10^{-11}$ erg s $^{-1}$ cm $^{-2}$ )	Flux (15–40 keV)* ( $10^{-11}$ erg s $^{-1}$ cm $^{-2}$ )	Energy Band $^{\dagger}$ (keV)	Reference $^{\ddagger}$
1998 May 9–11	<i>BeppoSAX</i> MECS+PDS $^{\S}$	0.79	2.4	15–40	1
2002 Dec. – 2006 Jun.	<i>INTEGRAL</i> ISGRI	2.11	3.2	17–60	2
2002 Oct. – 2004 Jan.	<i>INTEGRAL</i> ISGRI	1.80	1.9	20–40	3
2002 Oct. – 2004 Jan.	<i>INTEGRAL</i> ISGRI	1.98	1.5	40–100	3
2005 Dec. – 2006 Sep.	<i>Swift</i> BAT	4.6	5.3	14–195	4
2005 Nov. 10–13	<i>Suzaku</i> HXD PIN	...	2.4	15–40	5

Notes.

\* Fluxes in the 15–40 keV band calculated by assuming the best-fit complex absorber model shown in Table 3.

 $^{\dagger}$  Energy band used in the reference. $^{\ddagger}$  References: (1) Guainazzi et al. 1998; (2) Sazonov et al. 2007, Krivonos et al. 2007; (3) Beckmann et al. 2006; (4) Tueller et al. 2008 (5) This work. $^{\S}$  Model 6 in Guainazzi et al. (1998) (pure reflection plus single broad Gaussian model) was assumed.